Probabilistic Analysis of Distance Protection Accuracy in Power Grids Using Pandapower

Zhao Ming

Zhao Ming

539797

M.Sc. Information and Communication Systems / IMPICS

Master's Thesis

24.034

2025

Examiner: Prof. Dr.-Ing. Christian Becker

Zweitprüfer: Prof. Dr.-Ing. Arne Speerforck

Supervisor: Philipp Hube,

Masterarbeit   Datum: 13.02.2024

Probabilistische Analyse der Genauigkeit des Distanzschutzes in Stromnetzen mittels PandaPower

Als Folge des Umstiegs auf erneuerbare Energien werden große zentrale Kraftwerke durch kleinere dezentrale Erzeugungsanlagen ersetzt. Diese Erzeugungsanlagen sind vielfach über Umrichter an das Verteilnetz gekoppelt. Dabei werden Erzeugungsanlagen in bestehenden Netzen an unterschiedlichen Stellen beispielsweise über Stichanbindungen angeschlossen. Bisherige Netzschutzkonzepte können die Einspeisung erneuerbarer Energien einschränken, um die Schutzauslösungen sicherzustellen. Daher soll im Projekt VeN^{2}uS ein adaptives Netzschutzkonzept, das diesen geänderten Rahmenbedingungen Rechnung trägt, entwickelt werden. Dazu werden an dem Netzzustand angepasste Schutzparameter automatisch an die Schutzgeräte übermittelt. Um den Mehrwert dieses Konzepts gegenüber einem konventionellen Netzschutzkonzept darzulegen, muss auch berücksichtigt werden mit welcher Häufigkeit Fehler von Distanzschutzgeräten, die hauptsächlich betrachtet werden, auftreten. Bei diesen Fehlern kann es sich um sogenannte Über- und Unterreichweitefehler handeln.

In dieser Arbeit soll basierend auf unterschiedlichen Vorarbeiten ein Verfahren entwickelt werden, um die Häufigkeit der beiden Fehlertypen in einem betrachteten Testnetz probabilistisch zu bestimmen. Dafür sind Informationen über die erwarteten Verbräuche und Einspeisungen notwendig, die u. a. anhand von Wetterdaten und Lastprofilen prognostiziert werden sollen. Diese Daten werden dann für die stationäre Lastfluss- und Kurzschlussromberechnung verwendet, um die Über- und Unterreichweitefehler zu berechnen. Dazu sollen verschiedene probabilistische Verfahren erprobt und ein optimiertes Verfahren für Wahrscheinlichkeit der Fehler entwickelt werden.
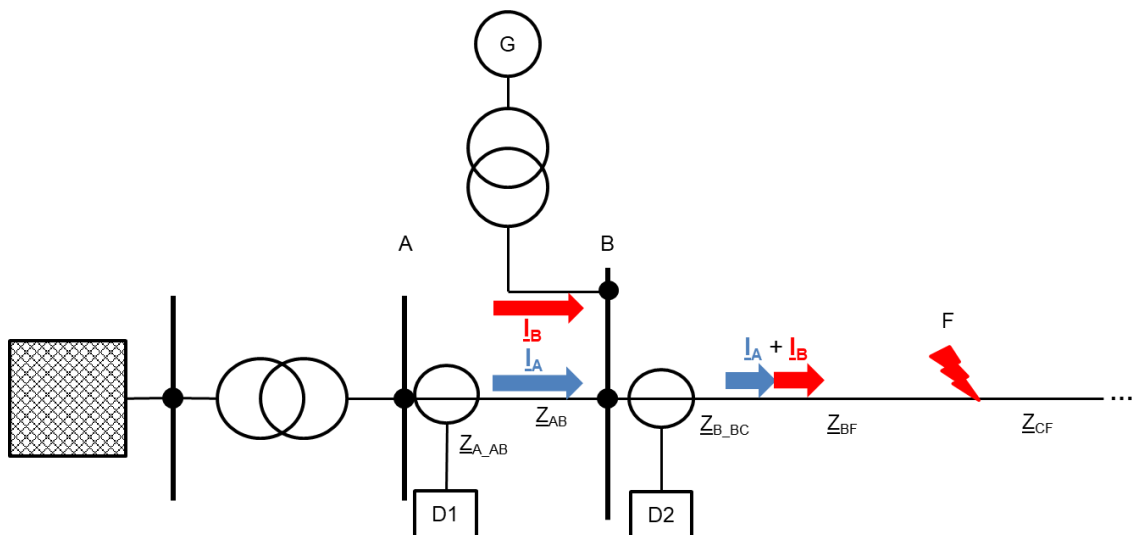

Abbildung 1 :Typische Situation für einen Unterreichweitefehler mit Zwischeneinspeisung

Folgende Strukturierung der Arbeit wird vorgeschlagen:

- Einarbeitung in die Thematik von Distanzschutzgeräten und deren Fehlern
- Einarbeitung in die vorliegenden Netzmodelle und die Berechnungsverfahren
- Recherche zum Thema probabilistischer Fehler
- Entwicklung eines Modells für die probabilistische Berechnung von Über- und Unterreichweitefehlern von Distanzschutzgeräten
- Bewertung der Ergebnisse und der generellen Anwendbarkeit des Verfahrens auf den Projektkontext

Im Anschluss an diese Arbeit ist in einem Vortrag über die Ergebnisse zu berichten.

Ansprechpartner: Philipp Hube Jan-Peter Heckel
Mail: philipp.hube@tuhh.de Mail: jan.heckel@tuhh.de

Kurzfassung

Der wachsende Strombedarf und die zunehmende Verbreitung dezentraler Erzeugungsanlagen verändern die Netztopologie und erhöhen den Bedarf an robusten Schutzstrategien. Der Distanzschutz als eine der traditionellen Schutzmaßnahmen ist nach wie vor ein interessantes Thema, dessen Vorteil die vergleichsweise geringen Kosten und die hohe Zuverlässigkeit sind. Herkömmliche Distanzschutzzoneneinstellungen sind normalerweise für radiale Systeme ausgelegt. Ihre Leistung kann durch Faktoren wie Zwischeneinspeiseeffekte, Leistungsschwankungen, hochohmige Fehler und dynamische Netzbedingungen beeinträchtigt werden.

Eine systematische Bewertung dieser Faktoren ist unerlässlich, um einen präzisen Betrieb von Distanzrelais in modernen Netzen zu gewährleisten. Frühere Studien übersehen häufig die langfristige Betriebsvariabilität, was ihre praktische Aussagekraft einschränkt. Durch die Quantifizierung und Visualisierung der Auswirkungen verschiedener Faktoren anhand von realen Last- und Erzeugungsprofilen kann die Arbeit die saisonalen Schwankungen der konventionellen Distanzschutzleistung analysieren und als Grundlage für den Vergleich fortschrittlicher Algorithmen dienen.

In dieser Arbeit wird die Leistung des Distanzschutzes bei probabilistischen Unsicherheiten in Bezug auf den Lastbedarf, die Winderzeugung und die Netzstärke bewertet. Im ersten Teil der Arbeit werden auf IEC 60909 basierende Kurzschlussberechnungsmethoden vorgestellt und analysiert, wie sich Parallelleitungen und Zwischeneinspeisungen auf die Genauigkeit des konventionellen Distanzschutzes auswirken, was dessen Grenzen in komplexen Netzen aufzeigt. Im zweiten Teil wird ein Rahmenwerk vorgestellt, das die Leistung des Distanzschutzes auf der Grundlage der Netztopologie des Pandapower-Typs festlegt, validiert und optimiert, sowie Methoden zur Verarbeitung von Last-/Windprofilen. Zur Bewertung der theoretischen Genauigkeit der zoneninternen Auslösung wird eine maßgeschneiderte

Distanzschutzklasse erstellt. Schließlich wird die Schutzleistung anhand von einjährigen Last-/Windprofilen bewertet.

Abstract

Growing electricity demand and increasing penetration of Distributed Generation (DG) are reshaping grid topologies, accelerating the need for robust protection strategies. Distance protection, as one of the traditional protections, is still an interesting topic with its advantage being comparatively low cost and good reliability. Conventional distance protection zone settings are normally designed for radial systems. Their performance can be affected by factors such as remote infeed effects, power swings, high-impedance faults, and dynamic grid conditions.

A systematic evaluation of these factors is essential for ensuring accurate distance relay operation in modern grids. Prior studies often overlook long-term operational variability, limiting their practical guidance. By quantifying and visualizing the impact of different factors using real-world load and generation profiles, the work is able to analyze the seasonal variation of conventional distance protection performance on High Voltage (HV) grids and serves as the baseline for the comparison of advanced algorithms.

This thesis evaluates the performance of distance protection accuracy under probabilistic uncertainties in load demand, wind generation, and external grid strength. The first part of the thesis introduces IEC 60909-based short-circuit calculation methods, and analyzes how parallel line and remote infeed affect conventional distance protection zone accuracy, showing its limitation in complex grids. The second part presents a framework that sets, validates, and optimizes distance protection performance based on Pandapower-type network topology, and methods for processing load/wind profiles. The customized distance protection class is constructed for evaluating the theoretical accuracy of in-zone tripping. Finally, this work evaluates the protection performance using one-year load/wind profiles.

Contents

Abbreviations

AC   Alternating Current

DC   Direct Current

HV   High Voltage

RMS   Root-Mean-Square

DWD   Deutscher Wetterdienst

IEEE   Institute of Electrical and Electronics Engineers

CIGRE   Conseil International des Grands Réseaux Electriques

Lowess   Locally Weighted Scatterplot Smoothing

IQR   Interquartile Range

SIPS   System Integrity Protection Schemes

DG   Distributed Generation

PMU   Phase Measurement Unit

ANN   Artificial Neural Network

Formula symbols

L_{arc}	Estimated length of the arc
L_{length_km}	Line length in kilometer
c	Voltage correction factor
c_{max}	Voltage correction factor for the maximum short-circuit current calculation
RX	Maximum resistance-to-reactance-ratio of the external grid
k	Ratio of the nominal to short-circuit current of the full converter element
I_{sc}	Short-circuit current
I_k''	Initial symmetrical short-circuit current
I_{kI}''	Short-circuit contribution of all voltage source elements
I_{kII}''	Short-circuit contribution of all current source elements
I	Network current matrix
I_k^{net}	Network current source injection matrix
$\underline{I}_{full\_converter}$	Current injection of the full converter element
I_{sgen}	Current injection of the static generator at steady state
I_{sgen}'	Current injection of the static generator at the initial fault state
I_{mag}	Magnitude of the current measurement at the protection device
ϕ_i	Current injection angle of the generator
$\phi_{\text{i\_angle}}$	Angle of the current measurement at the protection device
R_{arc}	Arc resistance in the fault loop
Y	Network admittance matrix
$\underline{Z}_{jj}$	Thevenin equivalent impedance seen at the fault node
Z	Network impedance matrix
$\underline{Z}_{line}$	Line impedance
$\underline{Z}_{ohm\_per\_km}$	Line impedance per kilometer
$\underline{Z}_{exgrid}$	External grid intern
$\underline{Z}_{L1}$	Impedance of line 1 or the primary line
$\underline{Z}_{L2}$	Impedance of line 2 or the secondary line
$\underline{Z}_{L3}$	Impedance of adjacent line of line 2
$\underline{Z}_{exg}$	Impedance of line 1

$\underline{Z}_{left}$	Impedance of left part
$\underline{Z}'_{left}$	Impedance of left part in another condition
$\underline{Z}_{right}$	Impedance of right part
$\underline{Z}'_{right}$	Impedance of right part in another condition
$\underline{Z}_{eq}$	Equivalent impedance
$\underline{Z}'_{eq}$	Equivalent impedance in another condition
$\underline{Z}_{load}$	Load impedance
$\underline{Z}_{gen}$	Generator impedance
$\underline{Z}_{apparent}$	Apparent impedance of the distance relay
$\underline{Z}_{zone1}$	Zone 1 of the distance protection device
$\underline{Z}_{zone2}$	Zone 2 of the distance protection device
$\underline{Z}_{zone3}$	Zone 3 of the distance protection device
$Z_{apparent\_mag}$	Magnitude of the apparent impedance
$\phi_{apparent\_angle}$	Angle of the voltage measurement at the protection device
$\underline{U}_{Ph\text{-}E}$	Phase to earth voltage
V_Q	Equivalent voltage source
V_N	Nominal voltage at the fault bus
V_n	Nominal voltage of the bus a component connects to
V	Network voltage matrix
V_{HV}	Nominal voltage level for the example network
$V_{prefault}$	Prefault voltage at the fault bus
V_{mag}	Magnitude of the voltage measurement at the protection device
ϕ_{v_angle}	Angle of the voltage measurement at the protection device
S_{sc_max}	Maximal short-circuit apparent power fed in from the external grid
S_{rated}	Rated power of the generator
P_{wt}	Mechanical power/active power captured/generated by the wind turbine
Q_{wt}	Reactive power produced by the wind turbine

1 Introduction

HV transmission networks form the backbone of modern power systems, delivering electricity over long distances with remarkable efficiency. The security and stability of these networks depend on protection devices to locate and isolate faults quickly. However, the growing complexity of these networks, driven by renewable energy integration, meshed topologies, and fluctuating load demands, has heightened their vulnerability to cascading failures. Even minor misoperations of protection devices can trigger large-scale disruptions, as demonstrated by historical lessons.

A striking example is the European blackout on November 4, 2006, which affected millions across the continent. The incident was initiated by a routine transmission line disconnection over the River Ems in Germany. However, the resulting power flow changes with disturbances, the disconnection and reconnection of loads and generators, leading to overcurrent protection and regional blackouts [1].

Similarly, on September 2, 2022, in the Netherlands, a heatwave caused by overheating conductors spread across substations, yet protection relays delayed tripping for approximately 4.5 minutes, exacerbating equipment damage [2].

These incidents underscore the need to validate grid operation and evaluate protection methods. Many studies have been conducted in the field of performance evaluation. In [3], the authors developed an evaluation platform that automatically analyzes fault records to estimate fault characteristics and protection performance. In [4], operational evaluations of existing System Integrity Protection Schemes (SIPS) in India are presented, and an algorithm is proposed to improve the system reliability under various operational scenarios. In [5], the authors present an analytical methodology for reliability assessment and failure analysis in a distributed power system.

However, these studies primarily focus on post-fault performance evaluation of existing protection installations. Additionally, most evaluation platforms can not easily integrate different protection installations within a network for comprehensive validation and performance comparison.

To address the limitation, this thesis advocates for an evaluation platform with three critical attributes:

- Applicability: The ability to model grid dynamics (e.g., load variations, DG variability) and simulate fault scenarios (e.g., phase-to-phase faults, high-impedance faults) to assess protection performance.

- Accessibility: An open-source architecture to foster transparency, reproducibility, and collaborative improvement, avoiding vendor-specific limitations.

- Adaptability: Flexibility to adapt to different grid topologies, as well as evolving grid configurations (e.g., Direct Current (DC)-Alternating Current (AC) hybrid grids) and support the development of various protection methods.

The review in [6] systematically compares four power system simulation tools, highlighting their respective strength. Pandapower stands out due to its open-source flexibility, practical network parameterization, and built-in short-circuit simulation [7]. In addition, the tool is based on the Python environment, which includes extensive visualization libraries and data analysis toolboxes. While it lacks the convenience of prebuilt protection models found in tools such as GridSim [6], its flexibility allows for the implementation of customized protection logic through Python scripting. Therefore, this thesis adopts Pandapower as the platform for protection performance evaluation.

Meanwhile, among protection methods, distance protection remains a widely used and cost-effective solution in HV grids due to its reliability and adaptability [8], after the concept first came up 120 years ago. This method estimates the electrical distance to a fault by combining voltage and current measurements. It is also widely used in practice. Nowadays, many countries, such as Germany, use distance protection as one of the main protections for HV systems [9]. However, studies have shown that meshed grids with DG penetration present challenges for distance protection [10]. To the best of the author's knowledge, there are

no studies evaluating distance protection performance in this grid configuration using real-world operational profiles over a long period, let alone using Pandapower as the platform. This gap limits the ability to quantify relay misoperations (e.g., overreach/underreach errors) under realistic, fluctuating conditions.

1.1 State of the Art

1.1.1 Protection Systems in HV Power Grids

HV power grids employ diverse protection schemes, each designed with specific operational advantages. These methods are typically categorized by their underlying fault detection principles and communication methods [11]. In this section, some common protection methods are introduced, highlighting their trade-offs in cost, response time, and system complexity.

Overcurrent and Differential Protection

Overcurrent protection remains one of the most widely deployed methods in HV systems due to its simplicity and speed. It operates by detecting when current levels exceed predetermined thresholds. However, as the method is current-sensitive, a high impedance fault may not be detected. As a complement, differential protection compares currents entering and leaving a defined zone to accurately identify internal faults. While this method provides high sensitivity, it relies heavily on fast and reliable communication between relays, which not only increases the cost but also can be a limiting factor.

Distance Protection

Distance protection operates by measuring the impedance and comparing it with predefined protection zones. By incorporating both voltage and current measurements, it improves reliability over methods that rely solely on current thresholds. However, challenges such as remote infeed effects, power swings, and high-impedance faults can degrade its accuracy. To enhance its reliability, distance protection is often combined with pilot protection schemes, which utilize communication links between substations for more accurate fault identification. Recent advancements in this field have focused on improving zone grading techniques through mathematical optimizations and adaptive grading mechanisms. These

adaptive schemes adjust impedance thresholds dynamically based on system conditions, mitigating the impact of fault impedance and transient variations.

PMU-Based Approaches

Phase Measurement Unit (PMU)-based approaches are fast-respond and time-synchronized protection methods, offering improved accuracy and rapid fault detection. However, their reliance on communication networks may introduce latency issues, making them most effective as supplementary systems rather than primary protection methods. Some studies have been done to improve distance protection performance in collaboration with PMU. [12] discusses the cascading problem in the third zone of distance protection and presents a method to distinguish the fault condition with the help of PMU. Also, in [13], the authors explore how PMU integration enhances distance protection performance by mitigating transient misbehavior.

1.1.2 Improvements in Conventional Distance Protection

Conventional distance protection grading can only be applied to radial systems in general. However, researchers have been seeking to adapt distance protection to modern, complex grids. Enhancements in this area typically involve either correcting the apparent impedance to account for the infeed effect [14] and high impedance loops [15], or refining the zone grading rules [16], with some approaches adapting the grading based on real-time grid conditions [17].

Numerous studies have proposed improvements in distance protection. For example, [18] employs a virtual measured voltage vector to distinguish in-zone from out-of-zone faults, and further uses a predefined vector to restrain the high impedance fault impact. [19] presents a time-domain-based approach that achieves faster detection compared with PMU-based methods and validates its performance in multiple scenarios. [20] introduces a pilot-based scheme that updates the coverage of each zone and revises the shared information in communication, leading to better performance in meshed networks with high DG penetration. [21] offers an adaptive scheme that adjusts the measured impedance to account for DG contributions with no communication hardware required.

1.2 Research Objectives and Organization

The research is structured around two core tasks. First, it investigates the feasibility of using Pandapower, particularly the short-circuit simulation module, for the short-circuit analysis and the validation of distance protection performance. This involves projecting the test network into a Pandapower-type network model and customizing Pandapower to integrate distance protection logic into the model. Second, this work conducts a probabilistic analysis of zone-trip errors over one year under dynamic network conditions. It involves simulating a wide range of fault scenarios in a meshed grid with DG penetration configurations. By generating and analyzing fault data under various network conditions, the research quantifies the probability of misjudgments in fault zone identification and identifies factors contributing to these errors.

Through this structured approach, this thesis aims to evaluate the feasibility and advantages of employing Pandapower as a tool for protection schemes validation and provide quantitative insights into the performance of distance protection in complex networks. This work serves as a baseline for the future advancement of distance protection methods.

This thesis is organized as follows. Chapter 2 and Chapter 3 give the fundamental information for the work, especially short-circuit current calculation with IEC 60909 standards and conventional gradings of distance protection. In Chapter 4, an experiment framework is proposed, which describes the experiment flowchart, the grid topology, and the processing of the grid component profiles. The conducted four case studies are simulated and discussed in Chapter 5. Finally, Chapter 6 summarizes the thesis and gives the future step proposals.

2 Short-Circuit Analysis in Power Systems

Short circuits occur when a low-resistance connection forms between two or more conductors in a power system. This work focuses on three-phase short circuits, which are the most severe fault condition in power grids.

When a short circuit occurs, the current flows through a conductive path from the fault location to the system ground neutral. The total impedance of the fault loop, consisting of both system equivalent impedance and fault impedance, determines the fault current characteristic, which may vary according to the short circuit cause.

2.1 Arc Resistance

The term "arc resistance" is chosen instead of "fault resistance" because the two terms are sometimes used interchangeably, leading to confusion. Fault resistance is a broader term, consisting of three parts: arc resistance, tower-grounding resistance, and resistance from foreign objects in the fault path. Among these, the arc resistance and tower-grounding resistance are relatively predictable.

Tower-grounding resistance depends mainly on the soil characteristics and grounding methods. This value is designed to be kept low for good lightning protection, normally under $5\,\Omega$. The arc resistance can vary from $1\,\Omega$ to hundreds of ohms. Laboratory observations of arc behavior, such as those presented in [22], give a closer look into its nature.

Arc resistance can be understood in two contexts:

1. Physical arc resistance: Measured or estimated during real faults, influenced by arc length, current magnitude, and environmental conditions.

2. Compensated arc resistance: A design parameter for protection relays to account for arc effects in impedance calculations.

Several empirical formulas for estimating arc resistance have been proposed, such as the Washington Formula [23], Mason Formula [24]

$$R_{\mathrm{arc}} = \frac{1804 \cdot L_{\mathrm{arc}}}{I_{sc}},$$ (2.1)

where

1804 is the voltage level associated with the arc in volts

L_{arc} is the estimated length of the arc in meters

I_{sc} is the fault current in amperes

R_{arc} is the arc resistance in ohms

Blackburn and Elmore Formula [25] [26]

$$R_{\mathrm{arc}} = \frac{1444 \cdot L_{\mathrm{arc}}}{I_{sc}},$$ (2.2)

and the formula given by Zeigler in [27]

$$R_{\mathrm{arc}} = \frac{2500 \cdot L_{\mathrm{arc}}}{I_{sc}}.$$ (2.3)

These formulas all give practical suggestions on setting the arc resistance. They also share a common proportionality: $R_{\mathrm{arc}} \propto L_{\mathrm{arc}}/I_{sc}$. A comparative analysis of these methods is provided in [28]. Recent advancements, such as those in [29] and [30], improve accuracy by incorporating real-time arc dynamics and distributed parameter models.

This work assumes a fault as a conductor-to-ground fault, where the fault resistance is negligible. This simplification is made because the effect of arc resistance is not the focus of this work. However, to maintain generality, a nominal arc resistance compensation value of $5\,\Omega$ (recommended for $110\,\mathrm{kV}$ systems in [27]) is retained in relay settings. It is mainly for illustration purposes.

Although this work assumes negligible fault resistance for simplicity, arc resistance remains a critical factor in practical distance relay operation. To demonstrate its impact on distance protection measurements, Figure 2.1 analyzes a single-phase-to-ground fault scenario, with
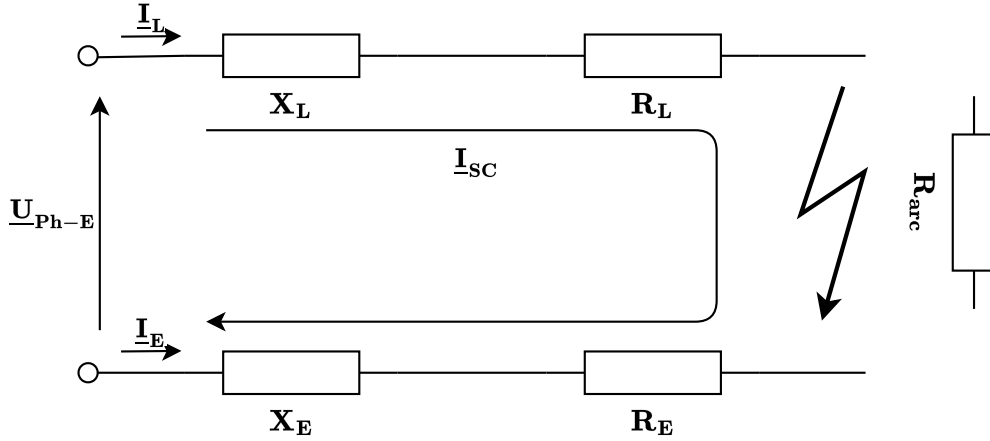
Figure 2.1: Single-phase-to-ground fault with arc resistance.

the resistance and reactance as well as the current of the corresponding transmission line section, arc section, and ground section marked in the figure.

This example builds on the knowledge of distance relay operating principles described in Section 3.1. With the loop, it can be derived,

$$\underline{U}_{\text{Ph-E}} = \underline{I}_L \cdot (R_L + jX_L) + \underline{I}_L \cdot R_{arc} - \underline{I}_E \cdot (R_E + jX_E), \tag{2.4}$$

yielding the apparent impedance:

$$\frac{\underline{U}_{\text{Ph-E}}}{\underline{I}_L} = (R_L + jX_L) + R_{arc} - \frac{\underline{I}_E}{\underline{I}_L} \cdot (R_E + jX_E), \tag{2.5}$$

so the resistive and reactive components become:

$$R_{\text{Ph-E}} = R_L + R_{arc} - \frac{\underline{I}_E}{\underline{I}_L} \cdot R_E \tag{2.6}$$

$$X_{\text{Ph-E}} = X_L - \frac{\underline{I}_E}{\underline{I}_L} \cdot X_E. \tag{2.7}$$

Here, the grounding fault impedance and the arc resistance introduce error into the apparent impedance.

For the distance protection, if there is no fault impedance, the faults should all fall in line with the ratio $\frac{R_L}{X_L}$ in the R/X plane. However, as Equations 2.6 and 2.7 show, there are two parts that need to be compensated: the ground part error and the arc resistance part error.

The ground part error will normally be taken into consideration beforehand, namely, the residual compensation factor in the relay. The arc resistance is compensated with a larger R-setting of the quadrilateral zones, with the value discussed in this section. A conservative enlarged R-setting estimation ensures faults with variable arc resistance remain within reach [27].

2.2 Short-Circuit Calculation Based on IEC 60909 Standards

The IEC 60909 standards (hereafter "the standard") are widely adopted for short-circuit analysis in three-phase AC systems. The 2016 revision of the standard introduced methods for handling converter-connected generators, further extending the coverage. This section outlines the key features of the standard, the definition of fault current components, and the methodology for applying the equivalent network approach in three-phase short-circuit calculations.

2.2.1 Key Features of the Standard

The standard is based on conservative assumptions to provide a practical methodology for short-circuit current calculation, and it has the following key features:

- **Fault current components decomposition**: It establishes a methodology for decomposing fault currents into components, capturing the key characteristics for designing short-circuit-related protection.

- **Equivalent network representation**: It gives steps for calculating the current by separately considering the voltage source and current source element contributions. Network elements are replaced with their internal impedance or current injections.

- **Worst-Case Conditions**: It assumes maximum generation and minimum load conditions to provide the lowest impedance path route, leading to the highest possible short-circuit current magnitude under this severe fault condition. Although the standard also provides procedures for calculating the minimum short-circuit current, our focus is on the maximum value since it is related to the distance protection design, while the minimum value is mainly related to overcurrent protection design.

- **Superposition method**: If the network condition is known before the fault happens, a more accurate short-circuit calculation can be done with the superposition method.

2.2.2 Fault Current Components

The introduction of fault current components is aimed at simplifying calculations. In real power systems, fault currents are complex and time-varying, influenced by factors such as generator dynamics, network topology, and system impedance. These currents exhibit complex waveforms, making direct analysis challenging [31].

By introducing fault current components, the standard simplifies calculations by reducing the need to model the full complexity of fault currents. Instead of modeling every transient detail, engineers can rely on these standardized values to design and test equipment, coordinate relays, and analyze system performance. Each short-circuit current has a time-varying waveform that can be reduced to a set of parameters so that it can be specified for equipment testing and suited for system calculations [32].

The standard defines three key components of fault currents:

- **Initial symmetrical short-circuit current** (I_k''): the maximal Root-Mean-Square (RMS) value of the AC component at the instant of fault occurrence, used for relay coordination.

- **Peak short-circuit current** (i_p): the maximum instantaneous fault current, critical for assessing mechanical stress on equipment.

- **Steady-state short-circuit current** (I_k): the RMS value of the AC component after transient effects have decayed, representing the sustained fault current.

In addition to these, the standard defines the symmetrical short-circuit breaking current (I_b). It is the RMS value of an integral cycle of the symmetrical AC component of the prospective short-circuit current at the instant of contact separation. I_b relates directly to the capability of the device to withstand fault currents at the moment of disconnection, ensuring safe and effective fault clearing.

Each of these components is carefully defined to reflect critical aspects of fault current behavior. The typical behavior of a short-circuit current is illustrated in Figure 2.2a [33], with

introduced components: I_k'', i_p, and I_k marked. The waveform consists of a decaying DC component and a constant AC component. Over time, the DC component, starting with an initial amplitude A, decays to zero due to system damping, while the AC component remains constant and stabilizes at the steady-state short-circuit current.

In addition, [34] discusses the impact of the arc voltage and calculation of unbalanced fault current, which are not covered in the standard. [35] gives the comparison between the theoretical results and the real data in an island operation.

These components show different characteristics when the fault occurs close to generators, as illustrated in Figure 2.2b. Near a generator, the AC decreases over time due to the time-varying reactance of the generator. If the DC time constant of a synchronous machine is larger than the subtransient time constant, the decaying short circuit can reach zero for the first time. In contrast, far from the generator fault, the AC component remains unchanged. For distance protection settings, the most relevant is I_k''. The following content will therefore focus on the calculation of I_k''.

(a)

(b)
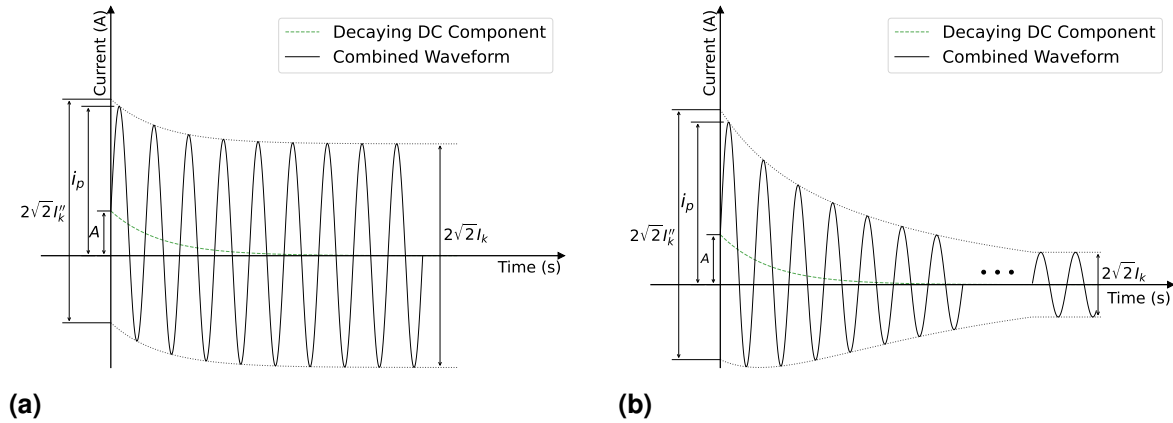
Figure 2.2: Time behavior of the short-circuit current: (a) far from the generator fault, (b) close to the generator fault.

2.3 Modeling Techniques

The initial short circuit is calculated in two stages:

- Calculate the short-circuit contribution I_{kI}'' of all voltage source elements.

- Calculate the short-circuit contribution I_{kII}'' of all current source elements.

The overall initial short-circuit current is the sum of the two-stage results $I_K'' = I_{kI}'' + I_{kII}''$. First, having a look at the voltage source contribution, all voltage sources, such as synchronous generators and external grids, are replaced by one equivalent voltage source V_Q at the fault location. The magnitude of V_Q is determined by:

$$V_Q = \frac{c \cdot V_N}{\sqrt{3}}, \tag{2.8}$$

where

c is the voltage correction factor

V_N is the nominal voltage at the fault bus

The voltage correction factor c depends on the system voltage level, the tolerance level, and the type of short-circuit current (maximal or minimal). It has a recommended value of 1.1 at the voltage level $110\,\text{kV}$ for the maximum short-circuit current calculation ($c_{max} = 1.1$). Meanwhile, all current voltage sources are treated as open-circuit. All active components are replaced by their internal impedance. The impedance values will be introduced in Section 2.3.1. Assuming the network consists of a total number of nodes n, and then for the calculation of the short circuit at the bus j, there is a linear relationship between the node voltage and the node currents:

$$I = Y \cdot V \tag{2.9}$$

For the voltage source contribution, only the fault node has a nonzero current injection:

$$
\begin{bmatrix} 0 \\ \vdots \\ \underline{I}_{kIj}'' \\ \vdots \\ 0 \end{bmatrix}
=
\begin{bmatrix} \underline{Y}_{11} & \cdots & \cdots & \underline{Y}_{1n} \\ \vdots & \ddots & & \vdots \\ \vdots & & \ddots & \vdots \\ \underline{Y}_{n1} & \cdots & \cdots & \underline{Y}_{nn} \end{bmatrix}
\begin{bmatrix} V_1 \\ \vdots \\ V_{Qj} \\ \vdots \\ V_n \end{bmatrix}
\tag{2.10}
$$

With the inversion method:

$$V = Y^{-1} \cdot i \tag{2.11}$$

$$
\begin{bmatrix} V_1 \\ \vdots \\ V_{Qj} \\ \vdots \\ V_n \end{bmatrix}
=
\begin{bmatrix} \underline{Z}_{11} & \cdots & \cdots & \cdots & \underline{Z}_{1n} \\ \vdots & \ddots & & & \vdots \\ \vdots & & \underline{Z}_{jj} & & \vdots \\ \vdots & & & \ddots & \vdots \\ \underline{Z}_{n1} & \cdots & \cdots & \cdots & \underline{Z}_{nn} \end{bmatrix}
\begin{bmatrix} 0 \\ \vdots \\ \underline{I}''_{kIj} \\ \vdots \\ 0 \end{bmatrix}
\tag{2.12}
$$

Take the jth row of the results

$$\underline{I}''_{kIj} = \frac{V_{Qj}}{\underline{Z}_{jj}} = \frac{V_Q}{\underline{Z}_{jj}}, \tag{2.13}$$

where $\underline{Z}_{jj}$ is the Thevenin equivalent impedance seen at the fault node.

The next step is the current source contribution. Current source elements such as PV plants and wind power plants are considered. All voltage sources are short-circuited. Assuming within the network, there are m generators in some of the nodes. Define the current injection from the converter at node i as I^C_{ki}. The net injection is the sum of the current from the current source and the equivalent current "drawn" from the node to the ground. So the net injection vector I^{net}_k derives as

$$
I^{\text{net}}_{ki} = \begin{cases} -I^C_{ki} + I''_{kIIi}, & \text{if } i = j, \\ -I^C_{ki}, & \text{if } i \neq j. \end{cases}
\tag{2.14}
$$

The nodal voltage equation remains:

$$V = Z \cdot I^{net}_k \tag{2.15}$$

$$
\begin{bmatrix} \underline{V}_1 \\ \vdots \\ 0 \\ \vdots \\ \underline{V}_n \end{bmatrix} = \begin{bmatrix} \underline{Z}_{11} & \cdots & \cdots & \cdots & \underline{Z}_{1n} \\ \vdots & \ddots & & & \vdots \\ \vdots & & \underline{Z}_{jj} & & \vdots \\ \vdots & & & \ddots & \vdots \\ \underline{Z}_{n1} & \cdots & \cdots & \cdots & \underline{Z}_{nn} \end{bmatrix} \begin{bmatrix} -\underline{I}_{k1}^C \\ \vdots \\ -\underline{I}_{kj}^C + \underline{I}_{kIIj}'' \\ \vdots \\ -\underline{I}_{kn}^C \end{bmatrix} \tag{2.16}
$$

with the fault bus node voltage set to 0. The jth row yields:

$$
0 = \underline{Z}_{jj} \left(-\underline{I}_{kj}^C + \underline{I}_{kIIj}'' \right) - \sum_{\substack{i=1 \\ i \neq j}}^{n} \underline{Z}_{ji} \underline{I}_{ki}^C \tag{2.17}
$$

Solve for $\underline{I}_{kIIj}''$:

$$
\underline{I}_{kIIj}'' = \frac{1}{\underline{Z}_{jj}} \cdot \sum_{i=1}^{n} \underline{Z}_{ji} \underline{I}_{ki}^C. \tag{2.18}
$$

In summary, the matrix calculation transfers the individual current injections through the network impedance to determine their combined effect at the faulted node.

2.3.1 Equivalent Modeling of Components

This section gives some common component equivalent models related to the standard.

- **Transmission Lines**: Transmission lines are modeled using their equivalent impedance, obtained as

$$
\underline{Z}_{line} = \underline{Z}_{ohm\_per\_km} \cdot L_{length\_km}, \tag{2.19}
$$

  where $\underline{Z}_{ohm\_per\_km}$ is the impedance per kilometer and L_{length_km} is the line length.

- **External Grids**: An external grid is modeled as a voltage source with impedance. The impedance is obtained as:

$$
\underline{Z}_{exgrid} = \frac{c_{max} \cdot V_n^2}{S_{sc\_max}} \cdot \left(\frac{1}{\sqrt{1 + RX^2}} + 1j \cdot \frac{RX}{\sqrt{1 + RX^2}} \right), \tag{2.20}
$$

where S_{sc_max} is the maximal short-circuit apparent power fed in from the external grid, and RX is the maximum resistance-to-reactance-ratio.

- **Full-converter Generators**: the full converter element, such as PV plants, and type 4 wind power plants, are modeled as a current source [36]. The inductive short-circuit current is obtained as:

$$\underline{I}_{full\_converter} = k \cdot \frac{S_{rated}}{\sqrt{3} \cdot V_n} \cdot exp(1j \cdot -\phi_i), \tag{2.21}$$

where

k is the ratio of the nominal to short-circuit current

S_{rated} is the rated power of the generator

V_n is the nominal voltage at the connected bus

ϕ_i is the current injection angle

- **Loads**: Loads and shunts are disregarded. The reason behind it can be seen from the key features of the standard. The short-circuit studies aim to determine the worst-case scenarios for fault currents. It is assumed that the maximum fault current is produced with low-impedance paths provided by generators, transformers, transmission lines, and so on. So, load, with a normally higher impedance, should not be considered.
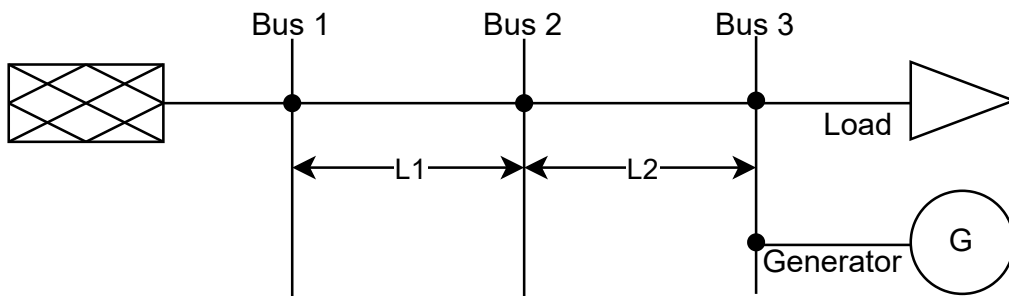
Figure 2.3: Network of explaining short-circuit calculation with the fault bus at Bus 2.

2.3.2 Superposition Principle

In many practical applications, the short-circuit analysis relies on simplified network models that neglect actual pre-fault operating states. While computationally efficient, this approach introduces limitations: For example, in systems where dynamic load behavior is the primary variable, this approach fails to capture load-driven variations in fault current magnitude.

In [37] different standards for short-circuit current calculation are compared and conclude that the superposition method in the standard yields results closer to reality. The superposition principle involves the following steps in addition to the previous method:

- Running a load flow calculation before the onset of the short circuit to obtain the pre-fault bus voltages and line currents.

- Replacing the previous equivalent voltage source with an equivalent voltage that reflects the pre-fault condition.

- Integrating loads and DG units into the network impedance matrix.

To explain the difference between classical and superposition-based principles, consider the radial network in Figure 2.3, where a short circuit occurs at bus 2. All buses have a nominal voltage level of V_{HV}.

The Classical Principle

The equivalent network impedance seen from bus 2 can be represented as two parts. The left part comprises the grid equivalent impedance $\underline{Z}_{exg}$ and line impedance $\underline{Z}_{L1}$, yielding:

$$\underline{Z}_{left} = \underline{Z}_{exg} + \underline{Z}_{L1}, \tag{2.22}$$

and the right part considers only line impedance $\underline{Z}_{L2}$, neglecting the load and generator:

$$\underline{Z}_{right} = \underline{Z}_{L2}. \tag{2.23}$$

Based on the classical method, the equivalent impedance is the parallel combination:

$$\underline{Z}_{eq} = \underline{Z}_{left} || \underline{Z}_{right}. \tag{2.24}$$

The current contribution comes from the grid and the generator, leading to the initial current calculation

$$I_K'' = I_{KI}'' + I_{KII}'' = \frac{c_{max} \cdot V_{HV}/\sqrt{3}}{Z_{eq}} + I_{sgen}, \tag{2.25}$$

where I_{sgen} represents the steady-state current of the generator.

The Superposition Principle

The superposition principle considers the prefault condition vector instead of the virtual source vector. The left part now reflects the prefault equivalent external grid impedance $\underline{Z}_{exg}'$, yielding:

$$\underline{Z}_{left}' = \underline{Z}_{exg}' + \underline{Z}_{L1}, \tag{2.26}$$

and the right part considers line impedance $\underline{Z}_{L2}$, load impedance $\underline{Z}_{load}$, and generator impedance $\underline{Z}_{gen}$, considering prefault voltage, yielding:

$$\underline{Z}_{right}' = \underline{Z}_{L2} + \underline{Z}_{Load}||\underline{Z}_{gen}. \tag{2.27}$$

The total Thevenin equivalent impedance changes to:

$$\underline{Z}_{eq}' = \underline{Z}_{left}'||\underline{Z}_{right}'. \tag{2.28}$$

The initial fault current is calculated using the prefault voltage $V_{prefault}$ at bus 2:

$$I_K'' = I_{KI}'' + I_{KII}'' = \frac{V_{prefault} \cdot V_{HV}/\sqrt{3}}{Z_{eq}'} + I_{sgen}', \tag{2.29}$$

where I_{sgen}' represents the initial fault current of the generator.

Through the calculation, it is clear that the superposition method requires the knowledge of the network conditions before the occurrence of the short circuit, which is not always feasible.

3 Distance Protection

3.1 Principles of Distance Protection

Distance protection is a protection scheme that determines the fault location along a transmission line by measuring the impedance between the relay location and a fault. Specifically, the distance relay uses locally measured voltage $\underline{V}$ and current $\underline{I}$ to calculate the distance, for balanced three-phase faults, following the basic relation

$$\underline{Z}_{\text{apparent}} = \frac{\underline{V}}{\underline{I}} = \underline{Z}_{ohm\_per\_km} \cdot L_{length\_km}, \tag{3.1}$$

under the assumption that the line impedance per unit length is constant (and neglecting fault resistance).

Distance protection can serve both as primary protection and as backup protection because it determines the tripping time according to the distance to the fault point. This ensures that the protection device closest to the fault point operates first to isolate the faulty line.

Typically, three protection zones are configured, with zone 1 as primary protection, and each zone having a specific time delay. The relay compares the measured $\underline{Z}_{\text{apparent}}$ with the zone boundaries defined by a polygonal characteristic, illustrated in Figure 3.1. A simple tripping rule is that the first calculated $\underline{Z}_{apparent}$ lies within "Zone 2", so the relay will wait for the preset time delay before tripping. The result $\underline{Z}'_{apparent}$ does not lie within any zone, so no tripping occurs.

The accuracy of impedance measurement in distance protection is influenced by several factors. Variations in line impedance, often due to bad environmental conditions, can change the effective impedance along the line. In addition, the performance of current and voltage
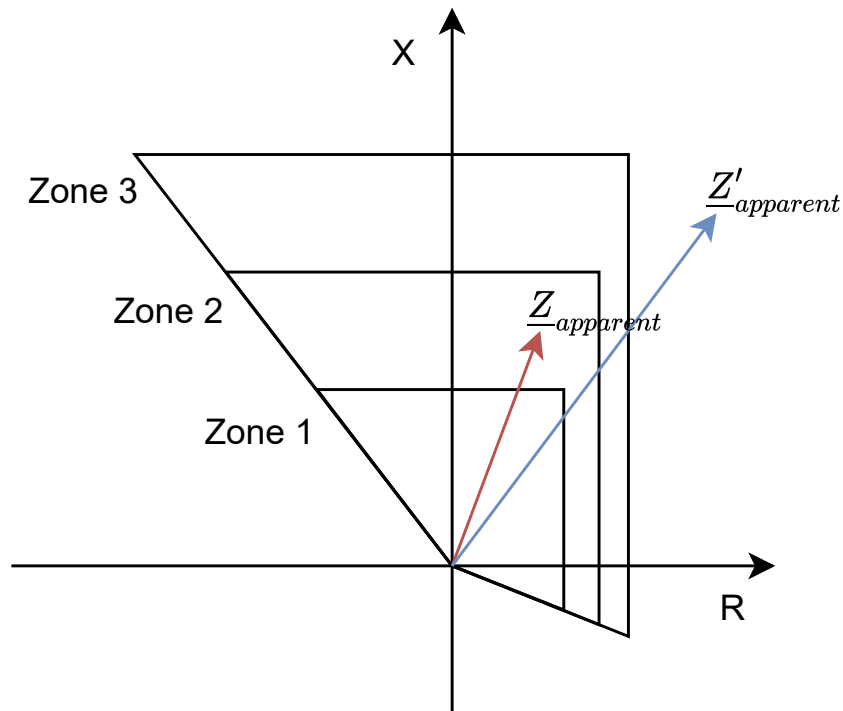
Figure 3.1: Illustration of zones in distance protection relays.

sensors, as well as transient measurement errors, may further distort the measurement. More factors will be explained in Section 3.2.

The measurement may lead to two types of errors:

- **Overreach error**: When the measured impedance is lower relative to the true relay-to-fault distance, leading to tripping for faults outside the desired protection zone.

- **Underreach error**: When the measured impedance is higher relative to the true relay-to-fault distance, the relay fails to detect a fault that is within the intended zone.

3.2 Grading of Distance Protection

To ensure both selectivity and coordination, distance protection schemes are typically divided into multiple zones. A common approach uses three zones:

- **Zone 1 (Primary Protection)**: This zone typically covers 80–90% of the protected line. The coefficient of 0.9 is employed when the network parameter is precisely documented and to avoid overreach in meshed networks [27]. So the first zone is designed as the major portion of the primary line plus the arc resistance compensation, as depicted:

$$\underline{Z}_{\text{zone1}} = 0.9 \cdot \underline{Z}_{L1} + R_{arc}, \tag{3.2}$$

  where $\underline{Z}_{L1}$ is the impedance of the primary line, R_{arc} is the compensated arc resistance.

- **Zone 2 (Backup Protection)**: This zone extends coverage to the remaining portion of the primary line and part of the adjacent line. A typical setting is:

$$\underline{Z}_{\text{zone2}} = 0.9 \cdot (\underline{Z}_{L1} + 0.9 \cdot \underline{Z}_{L2}) + R_{arc}, \tag{3.3}$$

  where $\underline{Z}_{L2}$ represents the impedance of the adjacent line section.

- **Zone 3 (Backup Protection)**: If zone 2 still cannot clear the fault properly, this zone serves as another backup protection, it covers the far end of the adjacent line. A typical setting is:

$$\underline{Z}_{\text{zone3}} = 0.9 \cdot \left(\underline{Z}_{L1} + 0.9 \cdot \underline{Z}_{L2} + 0.9^2 \cdot \underline{Z}_{L3}\right) + R_{arc}, \tag{3.4}$$

  where $\underline{Z}_{L3}$ is the impedance of a further adjoining line.

Figure 3.2 illustrates the zone coverage and associated time delays.

In a simple radial network, the settings are straightforward. However, in networks with parallel lines, multi-terminal configurations, or significant in-feed currents, additional considerations are necessary.

3.2.1 Branched Radial Network

The branched radial structure is the basic segment in the meshed network. For radial networks with branches, the settings of the three zones follow the shortest reach principle,
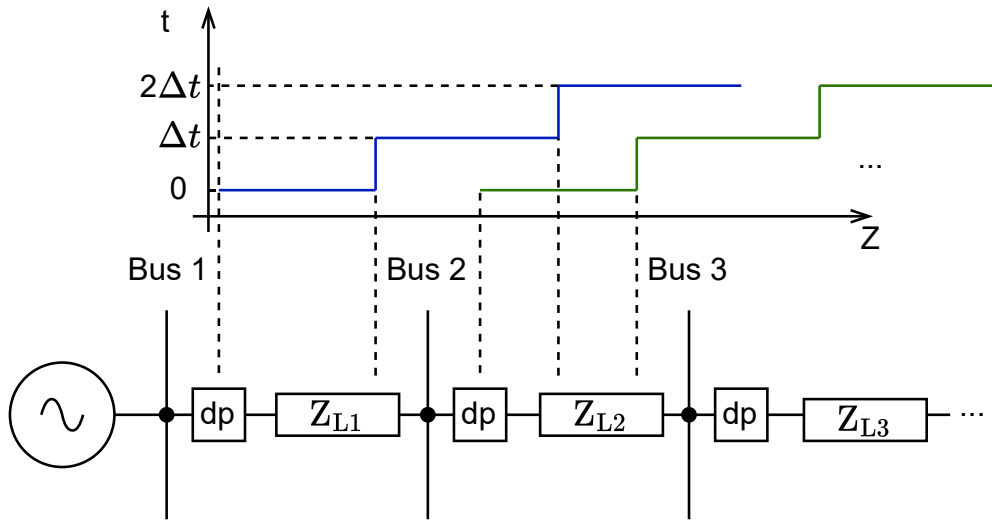
Figure 3.2: Illustration of zones and associated time delay in distance protection along the transmission line.

because, for one line segment, different distance protection devices should not have the same clearance time, ensuring proper fault clearance sequencing. In other words, it should be designed to correspond to different zones.

The design rule recommends that if several feeders are connected at the remote substation, the second zone of the upstream relay must be set to coordinate with the shortest first zone of the downstream relays present there. Similarly, the third zone is graded with the shortest second zone of those downstream relays [27]. The method adopted in this work is to convert the network as a tree structure (directed graph) with the bus where the relay is located as the root node and choose the shortest line in the depth 2 search and the depth 3 search for zone grading. This method avoids overreach into adjacent protections. Refer to Appendix A for feasibility validation.

3.2.2 T-connected Network and Multi-terminal System

In T-connected networks or multi-terminal systems, in-feed currents from adjacent buses can cause significant errors in the apparent impedance. For example, consider a fault occurring on a branch, and there is an infeed current from a static generator, as shown in Figure 3.3.
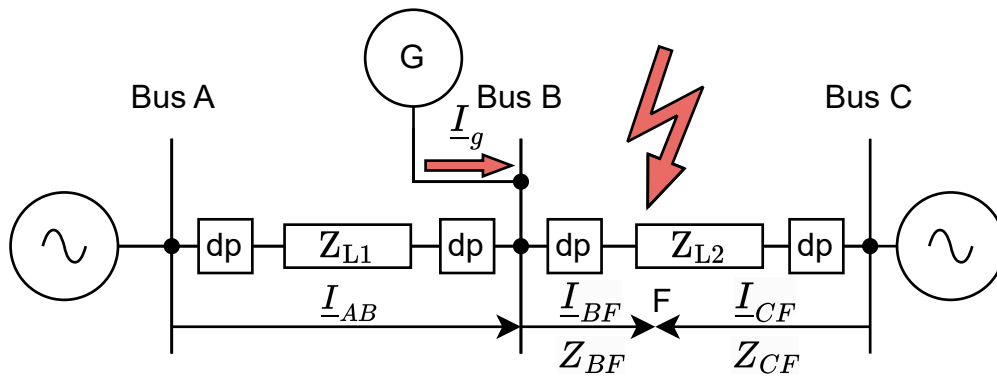
The relay at bus A (direction AB) measures:

$$\underline{V}_A = \underline{I}_{AB} \cdot \underline{Z}_{L1} + (\underline{I}_{AB} + \underline{I}_g) \cdot \underline{Z}_{BF} \tag{3.5}$$

can be rearranged as:

$$\frac{\underline{V}_A}{\underline{I}_{AB}} = \underline{Z}_{L1} + \frac{\underline{I}_{AB} + \underline{I}_g}{\underline{I}_{AB}} \cdot \underline{Z}_{BF}. \tag{3.6}$$

When the infeed current $\underline{I}_g$ has a positive magnitude, the infeed contribution increases the apparent impedance, potentially causing the relay to underreach [38].

Figure 3.3: Illustration of miscalculation related to the current source of infeed. $\underline{I}_g$ represents the equivalent short-circuit in-feed current contribution.

For the case of the multi-terminal line, the analysis is similar, and the fault current arrives from several sources, so the net fault current is the vector sum of currents coming from different directions. [39] draws the serious impact on distance protection, and some adaptive methods have been discussed in [15], [40].

3.2.3 Parallel Line Structure

In networks with parallel lines, factors such as mutual coupling [41], and additional current paths can distort the impedance measurement. Figure 3.4 gives one example, where the fault happens at one of the parallel lines. For the distance relay at bus A (direction AB), the

current relation will be:

$$\underline{V}_A = \underline{I}_{AB} \cdot \underline{Z}_{L1} + (\underline{I}_{AB} + \underline{I}_{CB}) \cdot \underline{Z}_{BF} \tag{3.7}$$

can be rearranged as :

$$\frac{\underline{V}_A}{\underline{I}_{AB}} = \underline{Z}_{L1} + \underline{Z}_{BF} + \frac{\underline{I}_{CB}}{\underline{I}_{AB}} \cdot \underline{Z}_{BF}. \tag{3.8}$$

The network structure is symmetric, when the fault location moves from bus B to bus C, the magnitude of the $\underline{I}_{CB}$ will see a shift from up to down and then up, with the direction changing. As Equation 3.8 indicates, it may introduce underreach or overreach errors in relay decisions.

If the network is one single source, the analysis is similar, and the apparent impedance will be the parallel connection of the impedance $\underline{Z}_{BF}$ and $\underline{Z}_{L2} + \underline{Z}_{CF}$ [27], which means the relay may only have underreach errors.
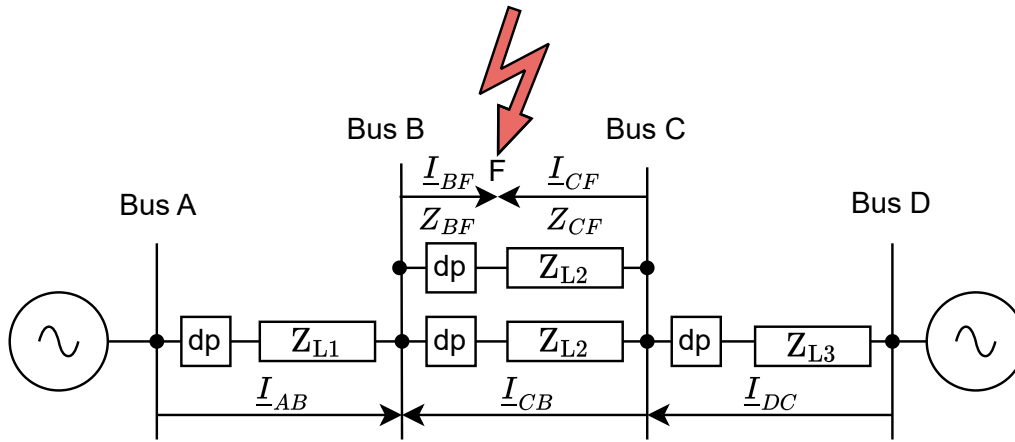
Figure 3.4: Illustration of miscalculations related to the parallel line. Variations in $\underline{I}_{CB}$ with the changing fault locations can lead to either overreach or underreach conditions.

Another example is given in Figure 3.5, where the fault happens at line 3. The focus remains at the same relay located at bus A (direction AB), the apparent impedance will be:

$$\underline{V}_A = \underline{I}_{AB} \cdot \underline{Z}_{L1} + \underline{I}_{BC\_up} \cdot \underline{Z}_{L2} + \underline{I}_{CF'} \cdot \underline{Z}_{CF'} \tag{3.9}$$

can be rearranged as:

$$\frac{\underline{V}_A}{\underline{I}_{AB}} = \underline{Z}_{L1} + \frac{1}{2}\underline{Z}_{L2} + \underline{Z}_{CF'}.$$
(3.10)

The result shows that when the fault path bypasses parallel lines, the relay will "see" the parallel line as the equivalent impedance together.

Move the focus to the relay located at one of the parallel lines (direction BC), for example, the line at the top, the apparent impedance will be:

$$\underline{V}_B = \underline{I}_{BC\_up} \cdot \underline{Z}_{L2} + (\underline{I}_{BC\_up} + \underline{I}_{BC\_down}) \cdot \underline{Z}_{CF'}$$
(3.11)

can be rearranged as :

$$\frac{\underline{V}_B}{\underline{I}_{BC\_up}} = \underline{Z}_{L2} + 2\underline{Z}_{CF'}.$$
(3.12)

This result indicates that the measured impedance can be significantly different from the actual line impedance if the contribution of the parallel branch ($\underline{I}_{BC\_down}$) is not properly accounted for.
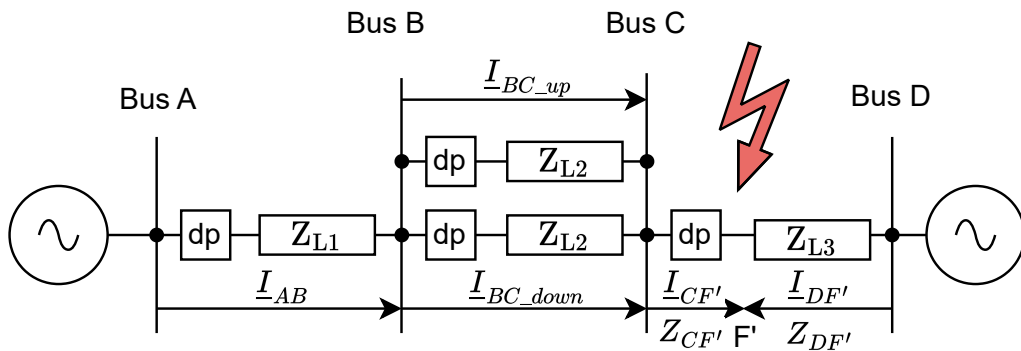
Figure 3.5: Another case of miscalculation related to the parallel line.

Figure 3.6 summarizes the various fault cases discussed above. These examples emphasize that the real fault distance may differ from the measured impedance due to unexpected topologies such as parallel lines and in-feed currents. Such discrepancies can lead to both overreach and underreach errors.
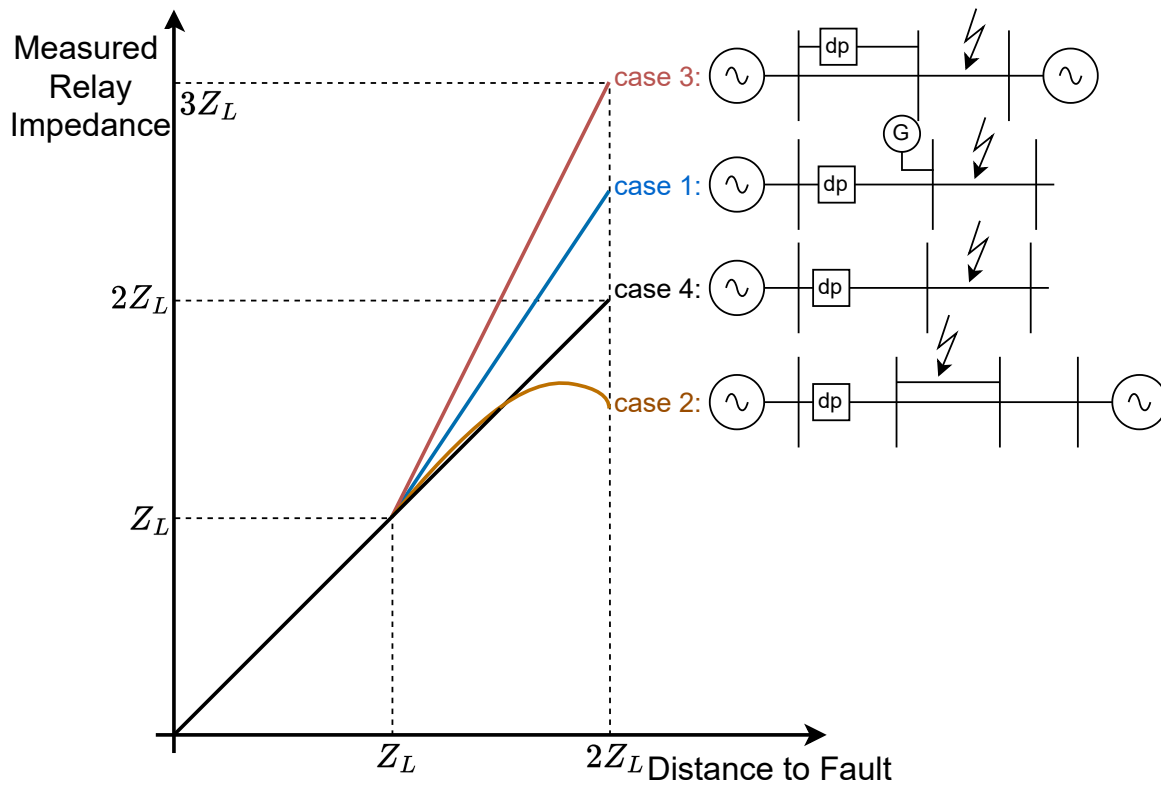
Figure 3.6: Summary of cases comparing the real relay-to-fault impedance and the measured apparent impedance. (All transmission line sections have an impedance of Z_L.)

3.2.4 Summary of Distance Protection Zone Settings

Distance protection zone settings require impedance data of the three hierarchical adjacent lines from the bus where the device is installed, as discussed earlier. Zone 1 serves as the primary fault protection, Zone 2 and Zone 3 function as two-stage backup protection in case of a Zone 1 failure. Each zone is designed to cover a significant portion of the protected line while avoiding overreach into adjacent zones. The principles correspond to the simple radial network settings outlined in Table 3.1.

More complex network configurations bring challenges into the zones setting for avoiding overreach or underreach errors, as pointed out in Figure 3.6. Several studies have addressed these issues [8], [42], [43]. It is a complex topic and beyond the scope of this work, therefore the recommended practical setting from [27] is applied, corresponding to the parallel line setting in Table 3.1. This setting applies to protection devices located in the configuration described as case 2 in Figure 3.6. The simple calculation accounts for shared

fault current paths by halving the adjacent line impedance contribution. For Zone 3, a 10% safety margin is applied, as recommended for high or extra high voltage grids.

Table 3.1: Grading principles summary for distance protection zones in different network configurations.

	Zone 1	Zone 2	Zone 3
Simple Radial Network	$0.9\underline{Z}_{L1}$	$0.9 \cdot (\underline{Z}_{L1} + 0.9\underline{Z}_{L2})$	$0.9 \cdot (\underline{Z}_{L1} + 0.9\underline{Z}_{L2} + 0.9^2\underline{Z}_{L3})$
Parallel Line	$0.9\underline{Z}_{L1}$	$0.9 \cdot (\underline{Z}_{L1} + 0.5\underline{Z}_{L2})$	$1.1 \cdot (\underline{Z}_{L1} + \underline{Z}_{L2})$

When the protection device is installed at the location in the configuration as described in case 3 in Figure 3.6, the apparent impedance leads to predictable underreach errors, indicated by the gap of measurements between case 3 and case 4. To compensate for this deviation, a correction factor of 2 is applied to the relevant segment.

3.3 Adaptive Distance Protection

Conventional distance protection, as defined in this work, operates using local measurements for apparent impedance and fixed zone settings that remain unchanged during grid operation. Instead, the adaptive protection method, as discussed in the state of the art, is designed to adapt the reach and tripping characteristic of distance relays in real-time, accounting for grid conditions. In this section, a glance at two aspects of adaptive distance protection enhancements is provided, serving as the foundation for future work.

Scholars have conducted many studies to implement adaptive distance protection. The two main methodologies are as follows:

1. **Adaptive Impedance Calibration**

   This method adaptively corrects for unintended apparent impedance errors caused by fault resistance, DG infeed, and so on. Studies such as [44] and [45] use phase relations at local measurements for more accurate impedance measurements. Advanced methods such as deploying the Artificial Neural Network (ANN) are exploited in [46] for correcting fault resistance contribution from apparent impedance error.

   Some other methods require information exchange between stations, where communication links between them need to be established. For example, in [20], the information between pairs is shared, and the tripping decision needs the participation of more than

one station. These methods effectively distinguish the in-zone and out-of-zone faults, but latency issues and the cost and reliability of communication links are not negligible.

2. **Adaptive Zone Adjustment**

This method adaptively adjusts the operation boundary of relays to account for grid topology changes and fault current variations. Studies such as [16] and [47] consider the ratio of fault current contributed by wind generators to reshape protection boundaries, aiming at eliminating underreach cases caused by infeed effects. Machine learning methods can also be exploited in this category. An ANN is trained in [48] to reshape the protection boundary into a flexible operating boundary.

These methods could prevent underreach of the unintended protection failure, but the protection range may overreach due to the adjustment, which is also not desirable.

4 Experiment Framework

4.1 Introduction to the Experiment Framework

Previous chapters have established the principles of distance protection for fault identification and clearance, alongside the challenges of accurate zone recognition in networks with complex topologies and variable in-feed currents.

A representative meshed network is researched, consisting of challenging parts such as parallel lines and wind in-feed. This chapter outlines the methodology to evaluate the performance of the conventional distance protection systems in the example network. The experiment addresses three objectives:

1. Quantify zone trip decision discrepancies in a static network.

2. Assess protection reliability with a fixed group of protection device parameters under realistic load and wind power generation fluctuations.

3. Validate the result-based optimization method for improving zone coordination.

The framework, as illustrated in Figure 4.1, consists of two interconnected analytical phases:

- **Static Network Analysis**

  A network model is first constructed using predefined static parameters of network components such as lines, external grids, loads, and wind generators. This Pandapower network model does not load time-variant components, so it is called a "static network". Distance protection devices are initialized with the conventional grading plan discussed in Section 3.2, where protection zones depend solely on network topology rather than operational dynamics.

This set of distance protection zone settings serves as the reference setting. The core function `simulate_faults_for_all_lines` evaluates protection responses under N-1 contingency scenarios across all transmission lines, generating baseline performance metrics, termed "static results". The function records the zone decision corresponding to the apparent impedance and the zone decision corresponding to the fault-to-relay distance, bound to the corresponding distance protection device. If the zone decisions give different results, then it is flagged as a "fault case".

- **Dynamic Network Analysis**

  A network model with a dynamic profile for load and wind generators is expected. The controller module in Pandapower enables time-series simulations, where load and generation profiles are updated through the controller `ConstControl` at a given time step. The network model with time series data loaded is termed a "dynamic network".

  The same fault simulation function `simulate_faults_for_all_lines` is executed for every time step. For each time step, if the zone decisions rise fault cases, the fault case number is recorded, termed "dynamic results". For a time span of 1 year, if the profile has a resolution of 10 minutes, the time step size will be in the order of 10000, so the complex record is no longer ideal.
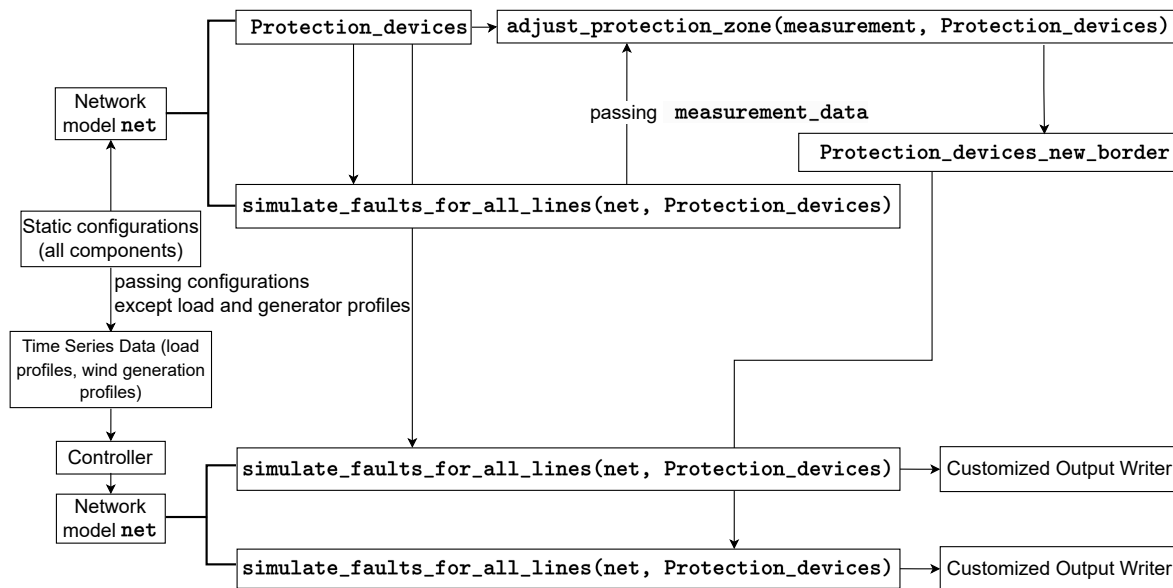
Figure 4.1: Experiment framework flowchart.

In the next step, the static results can be fed into the function `adjust_protection_zone` to update the protection zone boundaries, potentially reducing discrepancies in overall fault cases. These updated zone settings can be evaluated under both static and dynamic network configurations, and the latter is chosen in this work. The results will be compared with the original dynamic results. This approach demonstrates the feasibility of adaptive zone boundary adjustments using static results as a baseline. Although the methodology could support iterative updates (e.g., re-adjusting boundaries at each time step based on dynamic results), it is not the current implementation focus. Future extensions could explore real-time adaptation, but the present scope emphasizes methodological validation rather than algorithmic performance.

Several network variations can also be evaluated. First, a network configuration without wind generators is introduced to isolate and quantify the impact of wind infeed on the distance protection fault case ratio. Second, a network with a weak external grid is analyzed to demonstrate the effect of a common external factor on the fault case ratio. This scenario provides insights into the sensitivity of distance protection to external grid conditions.

The experimental framework uses Pandapower 2.14.11 [7] for network modeling, power flow calculations, and short-circuit simulations. The short-circuit calculations are performed using the IEC 60909 standard, as explained in Section 2.2. With Python support, net visualization, and result analysis are seamlessly integrated.

For the profile of the network components, two Python libraries are used, with load profiles derived from SimBench 1.5.3 [49] and wind generation profiles synthesized from wind speed data provided by Wetterdienst 0.97.0 [50].

The chapter is organized as follows: Section 4.2 describes the test network topology and static parametrization. Section 4.3 defines the distance protection hierarchy from initialization to fault decision making. Section 4.4 explains the data source and processing of load and wind generation profiles. Finally, Section 4.5 gives the explanation of the optimization algorithm adopted.

4.2 Test Network Topology

The test network adopted in this work, illustrated in Figure 4.2, is the 110 kV network segment [51] of a benchmark grid in the VeN^{2}uS project [52]. The reason for this choice is that, firstly, the network is a meshed HV grid including external grids, loads, and wind generator units that align with the dynamic design of power grid operation. Secondly, compared with the Conseil International des Grands Réseaux Electriques (CIGRE) or Institute of Electrical and Electronics Engineers (IEEE) test networks, this test network has a simple structure, but it contains typical structures and branch connections commonly found in distribution networks [51]. The parameterization of the test network follows the recommendation in [51]. Two external grids, connected at both ends of the network, ensure stability and balanced power flow. The static parameters are given in Table 4.1. ϕ_v is the angle of the voltage in the slack bus the external grid connects to.

Table 4.1: Network static parameters of external grids.

|	V_n (pu)	ϕ_v (degree)	S_{sc_max} (MVA)
External Grid A	1.018	1.7481	5000
External Grid C	1.002	1.4616	5000

Between bus A and bus B, there is a pair of parallel transmission lines. The line parameters are given in Table 4.2. The resistance, reactance, and conductance of the positive sequence and zero sequence are given.

Table 4.2: Network static parameters of the line parameters.

	R (ohm)	X (ohm)	C (nF)	R_0 (ohm)	X_0 (ohm)	C_0 (nF)
Line per km	0.0334	0.26	13.7	0.118	0.979	5.48

Wind power generation is integrated partly through busbar connections and partly through direct feed-in to the transmission lines as off-branch connections. The static parameters are given in Table 4.3. P and Q denotes the active power and reactive power of the power output at steady state.

As noted in [51], the location of onshore and offshore wind energy plants often makes it impractical to connect them via a dedicated busbar. Instead, they are typically added as intermediate feeders on existing lines using off-branch connections. This hybrid connection approach is retained to accommodate the varying geographical and grid constraints of wind
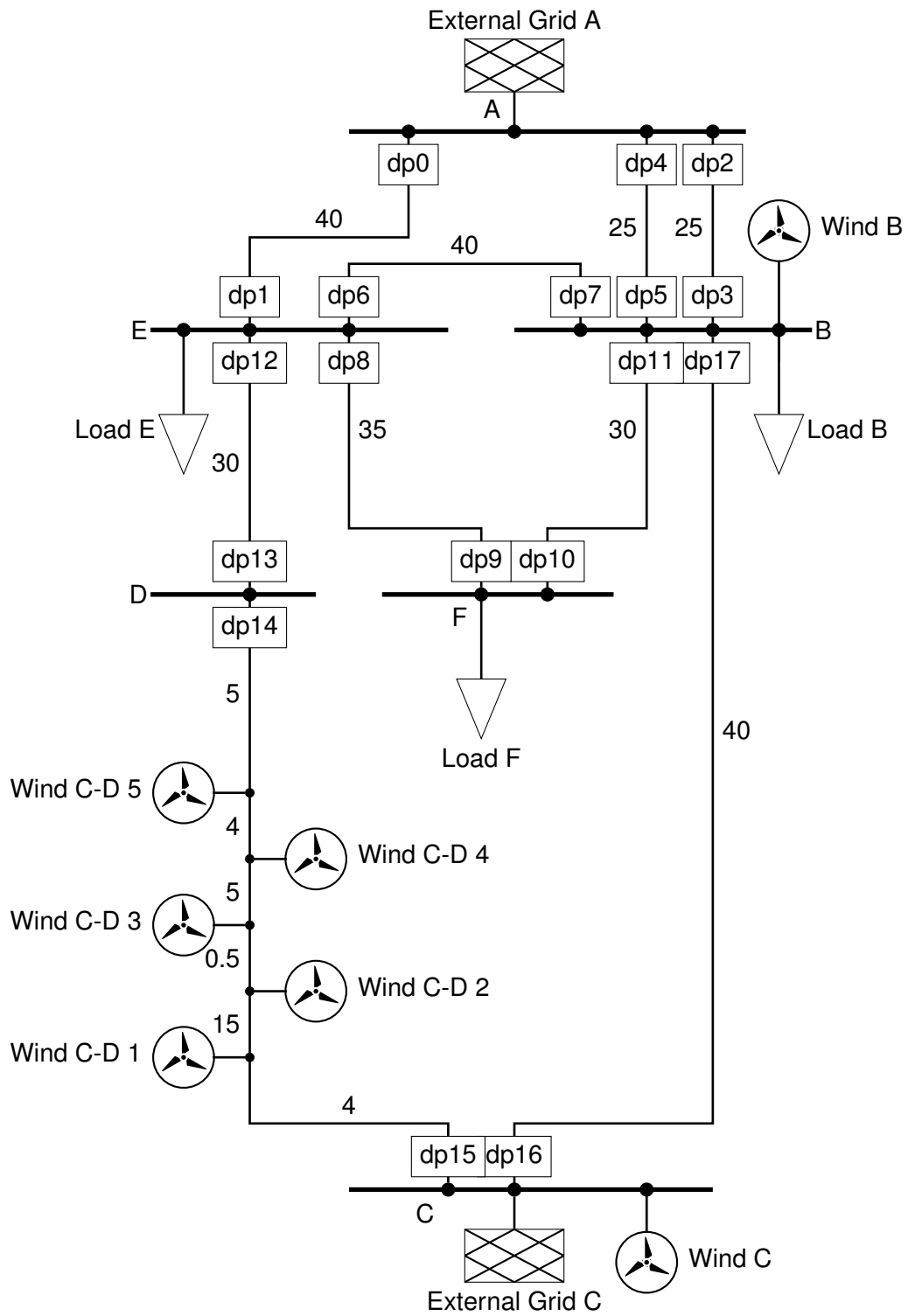
Figure 4.2: Test network structure and distance protection (dp) relay installation locations. (Line length unit: km)

Table 4.3: Network static parameters of wind farms.

	P (MW)	Q (MVar)	S_{rated} (MVA)	Generator type
Wind B	15	5	35	Current source
Wind C	35	5	50	Current source
Wind C-D 1	35	5	50	Current source
Wind C-D 2	20	4	35	Current source
Wind C-D 3	10	3	20	Current source
Wind C-D 4	50	10	75	Current source
Wind C-D 5	5	2	10	Current source

energy integration. It should be noted that the primary protected line for distance protection relays 14 and 15 is the same segment, between bus D and bus C.

The load is connected to bus B, bus E, and bus F. The static power consumptions are given in Table 4.4. P and Q denotes the active power and reactive power of the power consumption at steady state.

Table 4.4: Network static parameters of loads.

	P (MW)	Q (MVar)
Load B	200.00	65.74
Load E	200.00	65.74
Load F	100.00	32.87

For explanation purposes, the device number is also marked in Figure 4.2.

When performing the N-1 short-circuit test, the method is to always choose the short-circuit point at a fixed interval of 0.5 km on each line section. The midpoint is selected if the line length is less than 0.5 km.

4.3 Distance Protection Class Design

The Pandapower version used in this work (2.14.11) does not include a native distance protection module, although some papers have described its functionality for a future release [16]. Nevertheless, for this work, a custom distance protection class is implemented, with its core architecture illustrated in Figure 4.3.

4.3.1 Device Initialization

Each distance protection device is instantiated within the network, holding three identifiers:

- Device ID

- Associated bus ID (relay location)

- Associated line ID (protected line direction)

These identifiers uniquely determine the location of a device. For example, a relay positioned at bus A and oriented toward line AB is unique. Optional parameters, such as arc resistance compensation, can be included in this initialization as well.

During initialization, the relay accesses the network topology, with information such as line impedance, to calculate its protection zones following the grading principles outlined in Section 3.2. These boundaries are mapped to quadrilateral characteristics in the RX plane.

4.3.2 Apparent Impedance Measurement and Fault Cases Judgment

The class evaluates two impedance values during faults:

- Fault-to-relay impedance: The path from the relay to the fault location, considering the parallel line structure, is obtained through the Dijkstra algorithm [53].

- Measured apparent impedance: Derived from voltage and current measurements of short-circuit simulations.
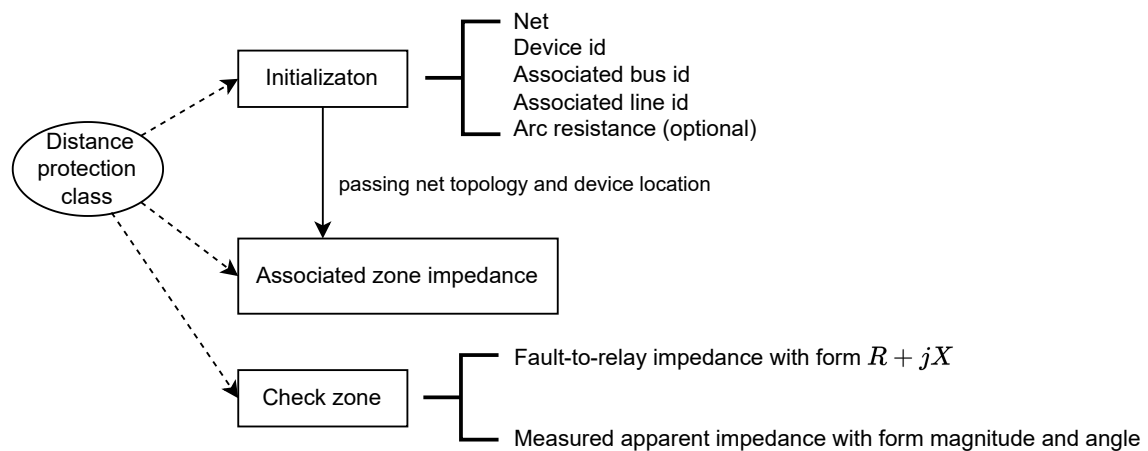
Figure 4.3: Distance protection class key architecture.

Based on the zone gradings derived in the previous step, these two impedance values lead to two zone decisions.

The impedance of the fault-to-relay path corresponds to a vector on the RX plane, which determines the reference zone decision. On the other hand, the apparent impedance determines the apparent zone decision of the relay. If the tripping zones pointed to by these two decisions do not match, it is considered that the relay has made an incorrect decision or the fault case.

Relying on the short-circuit simulation results, the measured impedance can be obtained as follows: The magnitude of the impedance is

$$Z_{\text{apparent\_mag}} = \frac{V_{\text{mag}}}{I_{\text{mag}} \cdot \sqrt{3}}, \tag{4.1}$$

where V_{mag} is the line-to-line voltage magnitude, and I_{mag} is the current magnitude. The $\sqrt{3}$ coefficient aligns with Pandapower native voltage and current measurements.

The angle of the impedance is

$$\phi_{\text{apparent\_angle}} = \phi_{\text{v\_angle}} - \phi_{\text{i\_angle}}, \tag{4.2}$$

where $\phi_{\text{v\_angle}}$ and $\phi_{\text{i\_angle}}$ are the angles of the voltage and current at the relay location, respectively. These values are used to determine the measured apparent impedance in the RX plane.

4.4 Load and Wind Generation Profiles

4.4.1 Introduction to SimBench and Load Profile Processing

SimBench is a research project to create grid models and time-series datasets for uniform comparison of innovative solutions in the field of network analysis, network planning, and operation [49]. The project offers detailed grid models across various voltage levels, from low-voltage to extra-high-voltage, along with corresponding time series data for loads, generation, and storage units. The valuable part for this work is the real-world load profile in HV, as the load profile in the HV grid is difficult to obtain.

Different SimBench datasets are distinguished by the grid code. The grid code used in this work is "1-HV-mixed–0-sw", with the code name denoting a modern HV grid with mixed-urban-rural characteristics. The dataset contains 58 different load profiles with a resolution of 15 minutes. The processing of the dataset includes aggregation and scaling to be consistent with the static load parameters of the test network.

Processing follows a three-step approach: First, power profiles are summed across all loads to capture system-wide demand patterns. Second, a scaling factor adjusts the average active power of the aggregated profile to align with the static load parameter. Third, the same scaling factor applies to the aggregated reactive power profile.

4.4.2 Introduction to Wetterdienst and Wind Data Processing

The Deutscher Wetterdienst (DWD), the German national meteorological service, provides open-access weather observations and forecasts through its climate data center. The datasets relevant to this section are the 10-minute resolution wind speed observation [54]. To facilitate programmatic access and spatial interpolation of these data, the work uses the open-source Python library Wetterdienst [50], which provides an interface for retrieving historical and real-time meteorological records. This library also employs a spatiotemporal interpolation algorithm (function `.summary(latlon)`) to estimate weather parameters, such as wind speed, at user-defined geographic coordinates where direct measurements are unavailable.

As the test network structure shows in Figure 4.2, there are a few wind farms in different locations, with their relative geolocation exposed. The first step is to obtain the geolocation where the wind turbines are located by projecting the grid network of wind farm locations onto a geographic map, with the network center aligned to central Hamburg coordinates.

Then for a target location (e.g., latitude 53.6°, longitude 10.3°), nearby weather stations within a user-defined radius (default 40 km) are identified and ranked by proximity, as illustrated in Figure 4.4. Time series data from these stations are aligned to a uniform temporal grid, resolving mismatches in sampling frequencies or missing data in the recording. It also prioritizes contributions from closer stations while requiring a minimum of four stations to

ensure robustness against outliers. Missing values are imputed iteratively using temporally adjacent measurements from the nearest valid stations.
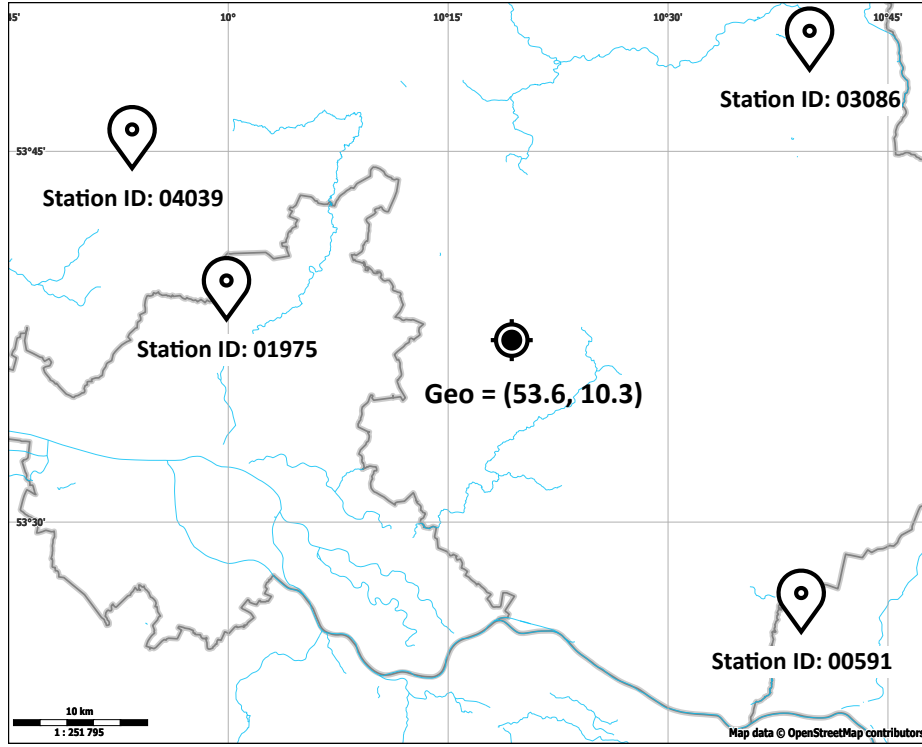
Figure 4.4: Illustration of the wetterdienst interpolation method. The wind speed data at the location $(53.6°\text{N}, 10.3°\text{E})$ is estimated using data from four nearby DWD stations. Station ID is the unique ID referred to German observation stations. Background Hamburg map comes from OpenStreetMap.

A one-year period wind speed series can be obtained as needed. The wind speed time series serves as the input for generating the corresponding wind farm power output.

The fundamental relationship between wind speed and ideal mechanical power capture is expressed as:

$$
P_{wt} = \begin{cases} 0 & \text{if } v_w < v_{\text{cut-in}} \text{ or } v_w > v_{\text{cut-out}} \\ c_P \cdot \frac{1}{2}\rho A v_w^3 & \text{if } v_{\text{cut-in}} \leq v_w < v_{\text{rated}} \\ P_{\text{rated}} & \text{if } v_{\text{rated}} \leq v_w \leq v_{\text{cut-out}} \end{cases} \tag{4.3}
$$

where v_w is the wind speed, A is the total area of the rotating blades capturing the wind, ρ is the air density, and c_P is the power coefficient, which is not fixed and quantifies the proportion

of available wind energy effectively harnessed by the turbine. The operational thresholds of the turbine, cut-in speed ($v_{\text{cut-in}}$), rated speed (v_{rated}), and cut-out speed ($v_{\text{cut-out}}$), determine the activation, rated power operation, and shutdown conditions, respectively. The power generation at the wind speed of v_{rated} is denoted as P_{rated}.

The air density is 1.225 kg/m at sea level at a temperature of 288 K. Other parameters are relevant to the specific wind turbine. The WWD-1 wind turbine specifications (manufactured by WinWinD, 1 MW model) give the parametrization of this model, as detailed in Table 4.5. The rotor diameter defines the swept area. The wind energy conversion coefficients and the associated wind turbine output curve are addressed in the Appendix B. Mechanical and electrical losses are considered by the manufacturer, so the relation between the active power and the wind speed is obtained.

A power factor is assumed to be set to a ratio of 0.3 between the active power and reactive power [55]. For the initial short circuit current calculation, this power factor value does not have a significant impact, as Equation 2.21 shows, because the real impact is on the prefault voltage vector.

Then the reactive power of the wind turbine is:

$$Q_{wt} = 0.3 \cdot P_{wt}. \tag{4.4}$$

For one location in the example network, the wind farm consists of a few wind turbines. The method is similar to how the load profile is processed. The active power of the wind turbine applies a factor so that the sum of the rated active power is aligned with the static active power there. For example, considering wind B in the network, it is designed to have 15 wind turbines with a rated active power of 1 MW.

Table 4.5: Wind turbine design parameters.

Type	3 blades, 4 degree tilt, up-wind
Rated power	1000 kW
Rotor diameter	56 m
Cut-in wind speed	3.0 m/s
Rated wind speed	12.5 m/s
Cut-out wind speed	25.0 m/s

4.4.3 Resolution Alignment of Time Series Data

The framework integrates load and wind generation profiles with different temporal resolutions: 15-minute resolution for load data and 10-minute resolution for wind generation. The load profile is linearly interpolated into a 10-minute resolution based on the time index of the data for synchronized simulations.

4.5 Protection Zone Optimization Algorithm

This section details the algorithm for optimizing protection zone boundaries, as shown in the flow of Algorithm 1. The algorithm recalculates the boundaries to minimize fault cases based on static results. The core method adapts the gradient descent algorithm [56], iteratively adjusting zone thresholds to minimize fault cases while avoiding local optima through a large iteration limit.

For each protection device, the algorithm processes static measurement data to evaluate underreach and overreach errors. These errors determine the adjustment direction, increase or decrease, for each zone boundary. A small perturbation is applied to the initial boundary value to test which direction reduces misjudgments (lines 5-8). If increasing the boundary lowers errors, searching continues upward; if decreasing works better, searching moves downward.

The iterative process updates the boundary in the chosen direction by a fixed step size (line 7). If misjudgments decrease, the new boundary is kept. If errors increase, the direction reverses, and the searching direction bounces back to explore the opposite direction (lines 10-15). This search continues until the maximum iteration count (default 100) is reached, ensuring sufficient exploration to avoid a local minimum. Throughout the process (lines 5-25), historical boundary values and their error counts are tracked to identify the best-performing candidate.

After testing all zones, the algorithm selects boundaries from the best-performing candidates in line 26, while at the same time, maintaining the required order $Zone1 < Zone2 < Zone3$. These boundaries are applied to the protection device and later validated in the dynamic network. The method balances accuracy with computational efficiency.

Algorithm 1 Adjust Protection Zone Boundaries with Measurement Data

---

Require: Measurement data: $measurement\_data$, Protection devices: $protection\_devices$
Ensure: Adjusted protection zones for each device

1: **for** $device$ in $protection\_devices$ **do**
2:     $device\_data \leftarrow$ Filter $measurement\_data$ for $device$
3:     $original\_boundaries \leftarrow$ Initial zone boundaries of $device$
4:     $boundary\_iter\_history \leftarrow$ store boundaries and their misjudgments for each zone
5:     **for** $zone\_index$ in zone index $range(0,3)$ **do**
6:         $boundaries \leftarrow original\_boundaries$
7:         $current\_boundary \leftarrow boundaries[zone\_index]$
8:         $direction \leftarrow$ Initial adjustment direction (up or down)   ▷ Give $current\_boundary$
    a perturbation and set the initial $direction$ and $current\_boundary$ based on the misjudg-
    ment result
9:         $best\_misjudgment \leftarrow$ Compute misjudgments with $current\_boundary$
10:        **while** $iteration < MAX\_ITERATION$ **do**
11:            $current\_boundary \leftarrow current\_boundary + direction * adjustment\_step$
12:            $new\_misjudgments \leftarrow$ Compute misjudgments with $current\_boundary$
13:            **if** $new\_misjudgments < best\_misjudgment$ **then**
14:                $best\_misjudgment \leftarrow new\_misjudgments$
15:            **else if** $new\_misjudgments > best\_misjudgment$ **then**
16:                $direction \leftarrow -direction$ ▷ Reverse adjustment direction
17:                **if** $direction = 1$ **then**
18:                    $current\_boundary \leftarrow \max(boundary\_iter\_history[zone\_index].keys()$
19:                **else**
20:                    $current\_boundary \leftarrow \min(boundary\_iter\_history[zone\_index].keys()$
21:                **end if**
22:            **end if**
23:        **end while**
24:        Store boundary value in $boundary\_iter\_history$ which has the $best\_misjudgment$
    as a candidate for $best\_boundary\_option[zone\_index]$
25:     **end for**
26:     $final\_boundaries \leftarrow$ Select candidate boundaries from $best\_boundaries\_option$ en-
    suring zone order: $Zone1 < Zone2 < Zone3$
27:     Update $device$ zone impedance with $final\_boundaries$.
28: **end for**
29: **return** Protection devices with adjusted zone boundaries.

---

5 Simulation and Results Discussion

This chapter presents a detailed discussion of the simulation results drawn from the two phases of the framework proposed in the previous chapter, and their implications for the application of conventional distance protection grading in complex networks.

The simulation is based on several assumptions for critical distance protection behaviors. For each protection relay, only three-depth adjacent lines are taken into consideration, meaning the analysis evaluates the performance of each device on its primary line and two backup lines. For example, the evaluation of the distance protection device 15 consists of the primary protection of line CD and backup protection across several lines (line DE, line EA, line EB, and line EF).

On top of that, if the external grid feeds into the fault path (the shortest fault impedance path) between the protection relay and the fault location, such cases are excluded from the simulation results. This is because the dominant fault current supplied by the external grid can overshadow local dynamics.

Additionally, the meshed network topology introduces a challenge where the apparent impedance measured by some relays may not always fall in the first (positive) quadrant of the RX plane, even when the fault is in the intended direction of protection. Such deviations, where the impedance point falls outside the expected quadrant, are also categorized as fault cases because it is still the behavior that the relay does not operate within its designated protection zones. The ratio of such occurrences is included in the results to serve as a design reference for distance protection.

5.1 Case Study Definitions

This section summarizes the researched case studies for better clarification in the results discussion. Four cases are defined based on configurable configurations of the network. The first is the presence of infeed currents from wind generators, allowing for scenarios with and without wind generation. The second is the external grid strength, which can be set as either a strong grid, as provided in the reference table (S_{sc_max} =5000 MVA), or a weak grid (S_{sc_max} =100 MVA). Last but not least are the distance protection parameters, which can either follow the conventional grading plan or be optimized using the proposed algorithm. When visualizing the current flow, static parameters are used to represent the grid conditions consistently.

The simulated cases are defined as follows:

- Case 1 (Baseline): Conventional grading plan parameters with wind generators and strong external grids connected.

- Case 2 (No wind generators): Conventional grading plan parameters without wind generators connected, retaining strong external grids.

- Case 3 (Weak external grid): Conventional grading plan parameters with wind generators and weak external grids connected.

- Case 4 (Optimized zones): Optimized grading parameters with wind generators and strong external grids connected.

5.2 Validation of Zone Settings Over a One-Year Period

The simulation results for Case 1, simulated over a one-year period, serve as the reference for evaluating the performance of the zone settings. The fault case ratio distribution in weekly resolution is presented in Figure 5.1. The results show a seasonal pattern with distinct differences between warm and cold seasons. Here, the warm season spans from week 14 to week 40, while the remaining weeks represent the cold season.

The median faults remain relatively stable throughout the year, with slightly higher values observed in the warm season. The Interquartile Range (IQR) shows the trend that the

range narrows during the warm season and is approximately 50% times wider during the cold season. Most data points fall within the IQR and outlier analysis reveals significant seasonal differences. The number of outliers in the warm season is approximately 3 times higher than in the cold season.

The observation suggests that warmer weeks introduce more extreme values, whereas colder weeks introduce more common fluctuations in fault case ratios.
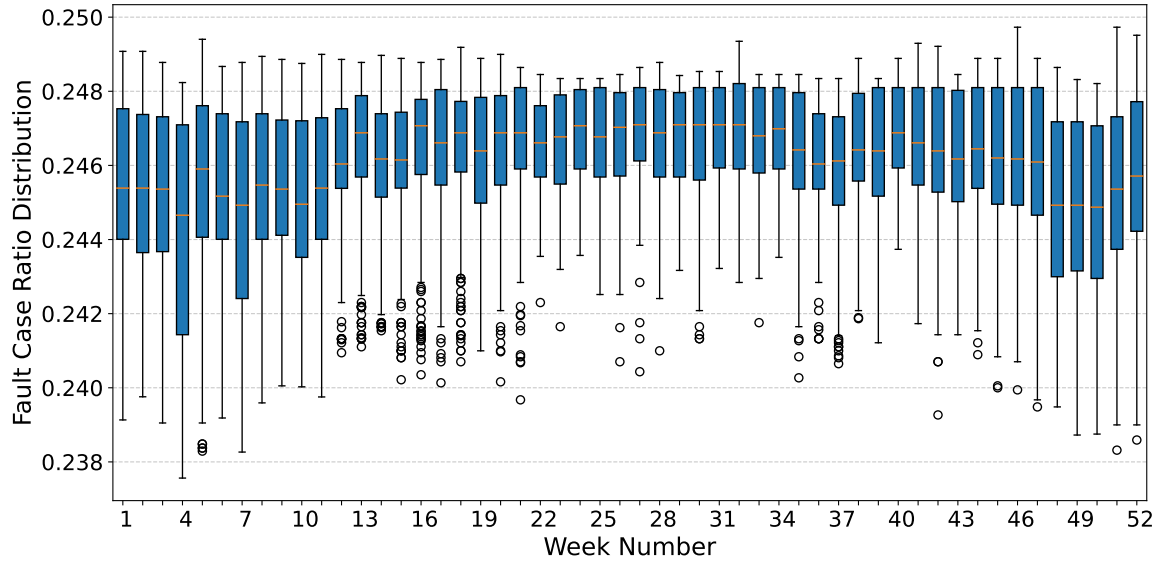
Figure 5.1: Distribution of fault case ratio (Case 1) over one year with weekly resolution. Boxplot elements show median (orange), IQR (box), and 1.5 ·IQR whiskers.

Figure 5.2 illustrates the average fault count distribution across different devices, along with the proportion of primary faults. The distribution of faults correlates strongly with the network topology. Devices within the core of the mesh network, where the endpoints of the primary line protected by the device are bus B and bus E in this network structure, account for 92% of all recorded faults.

The primary faults, which are the most unacceptable conditions, only happen in the wind farm tie-line area and represent only a minor fraction of the overall fault cases.

Additionally, faults with apparent impedance measurements that do not fall in the first quadrant of the RX plane account for approximately 17% of the total faults.
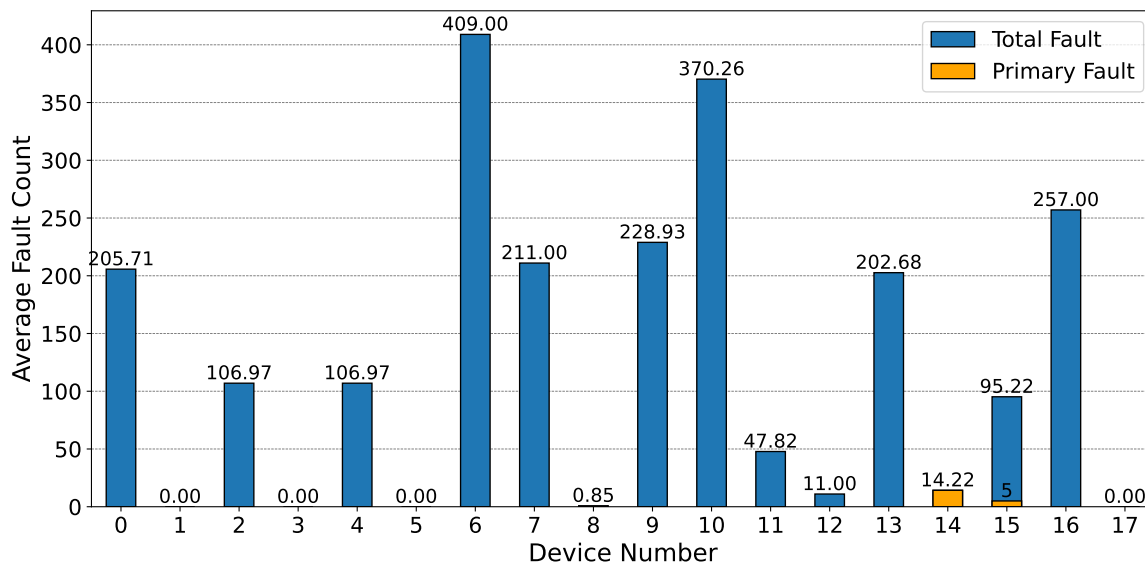
Figure 5.2: Average total fault case and primary fault case counts across devices.

5.2.1 Evaluation of Fault Behavior: Fluctuation of Fault Case Ratio

The seasonal characteristics of wind generation and the periodic behavior of load profiles provide the basis for analyzing fault case ratio fluctuations. The results in Figure 5.1 suggest a potential link between these factors and the observed seasonal outlier bursts and high-variance periods. Detailed load and wind generation profiles are provided in Appendix D.

To isolate the impact of these factors, two controlled scenarios are analyzed, described in Figure 5.3. Scenario 1 represents conditions with a higher loading impact, while Scenario 2 corresponds to increased wind generation. The profile generation method ensures that load trends remain consistent across both scenarios. Although wind generation patterns are not identical, the selected data points ensure that Scenario 2 features a significantly higher generation level, allowing a comparative analysis of low and high wind generation effects.

Scenario 1 indicates an increased likelihood of overreach faults under a higher loading condition. The explanation is based on theories and measurements. Higher loading can lead to a voltage drop at the relay location due to increased power flow through the resistive loading. The initial short-circuit current slightly increases due to the reduced equivalent impedance based on the short-circuit calculation method in Section 2.2. The relay perceives faults as closer than it should be, leading to potential overreach faults. Table 5.1 provides the short
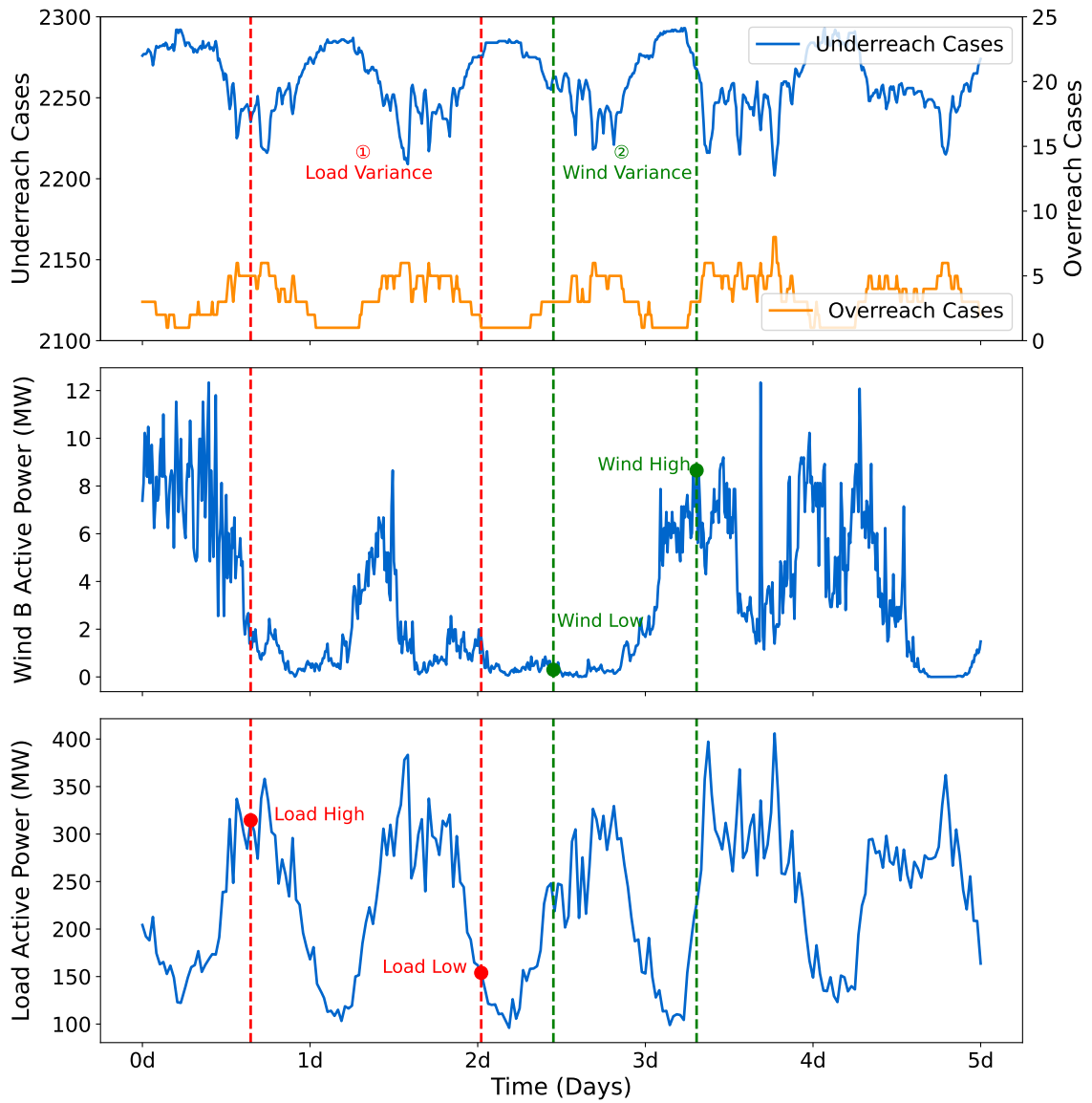
Figure 5.3: Impact of load and wind generation variations on distance protection performance. Scenario 1 represents a load variation case. Scenario 2 represents a wind variation case.

circuit results of the fault point located 0.25 km from bus B on line BE, in the two loading conditions of Scenario 1. The first column shows the initial short-circuit current, with a small increase in the higher loading condition. The other two columns show higher loading increases resistive losses in the grid, leading the equivalent system impedance towards the R axis, with the magnitude slightly decreased though.

Scenario 2 shows no obvious tendency toward either underreach or overreach case under a higher wind generation condition. The infeed current from higher wind generation, as Equa-

Table 5.1: The comparison of short-circuit simulation results at a fault bus under high and
low loading scenarios (Scenario 1). The fault bus is located 0.25 km from bus B
on line BE.

	I_{sc} (kA)	R_{eq} (ohm)	X_{eq} (ohm)
Higher loading	18.533555	0.935135	3.360297
Lower loading	18.285974	0.68423	3.513577

tion 3.6 indicates, may worsen the underreach case counts. But as the figure shows, it sug-
gests this small increase can not be observed. Table 5.2 compares the apparent impedance
measurements for device 2, with fault points at varying distances from bus B along line BC.
The results align with the observation, showing minor variations in apparent impedance be-
tween low and high wind generation scenarios. This is attributed to the relatively low fault
current contribution from inverter-based wind generators. Although the inductive nature of
wind farm infeed currents introduces a slight phase shift in the impedance trajectory, this
effect is insufficient to significantly impact protection performance.

Table 5.2: The comparison of apparent impedance measurements at different fault dis-
tances under low and high wind generation scenarios (Scenario 2). The parallel
line compensation is already applied in the referenced fault to relay impedance.
Impedance unit: ohm.

Distance (km)	Fault to relay impedance	Low generation	High generation
8.5	1.402+10.921j	2.134+12.291j	2.115+12.309j
8.75	1.419+11.051j	2.183+12.453j	2.164+12.472j
9	1.435+11.181j	2.233+12.614j	2.213+12.634j
9.25	1.452+11.311j	2.283+12.775j	2.262+12.796j

5.2.2 Evaluation of Fault Behavior: Which Devices Are Prone to Have Faults

The brief analysis of the distribution of fault case counts across devices in Figure 5.2 con-
cludes that devices situated within the meshed core of the network, especially those asso-
ciated with critical junction buses, face persistent challenges due to the interplay of complex
fault current paths, while devices whose fault paths undergo wind farm tie-line ares, face
moderate challenges. This pattern suggests that the interaction between fault current injec-
tions and network meshing significantly affects protection performance.

To illustrate the impact, consider a fault located at the center point of line BE, the initial
fault current flow with current magnitude and bus voltage is depicted in Figure 5.5. Take the

measurement disturbance of device 13, which is located at bus D in the direction of line DE, as an example. The apparent impedance seen by the relay follows

$$\underline{Z}_{apparent} = \underline{Z}_{DE} + \frac{\underline{I}_{E-fault}}{\underline{I}_{DE}} \cdot \underline{Z}_{E-fault}, \tag{5.1}$$

where $\underline{Z}_{E-fault}$ and $\underline{Z}_{DE}$ represents the fault current from bus E and current in line DE, respectively, and $\underline{Z}_{E-fault}$ and $\underline{Z}_{DE}$ denote the corresponding impedance. The contribution of the infeed causes the impedance of the segment from bus E to the fault location ($\underline{Z}_{E-fault}$) to be approximately 3 times considered in the measurement. But the infeed can only affect the backup zones, the primary zone protection therefore is not affected.

Compared with the infeed effect of the external grid, the fault case ratio related to the wind infeed is less extreme. The inverter-based nature of wind generators limits their fault current contribution compared with the conventional synchronous sources. Figure 5.4 shows the initial current flow in line CD while the fault is located at the midpoint of the branch between wind C-D 4 and wind C-D 3. The infeed error increases step by step with the joined infeed current of wind generators. However, the magnitude increase does not even exceed 20%, which is definitely less pronounced to see in the fault number compared with the one related to meshed network infeed.
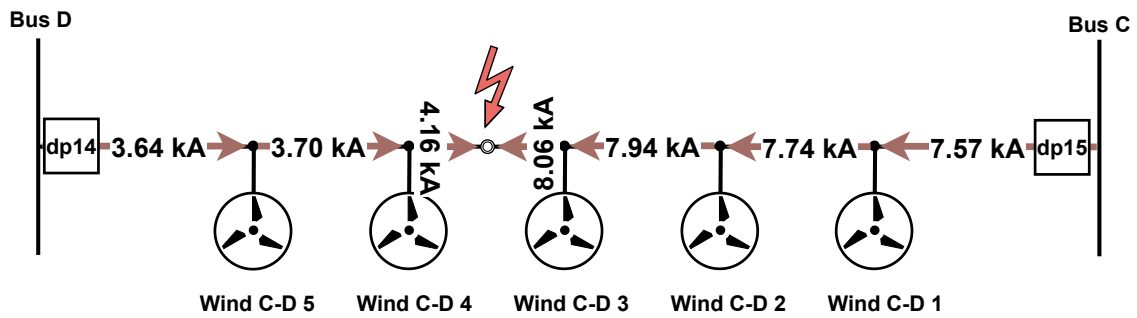
Figure 5.4: Visualization of initial short-circuit current flow with the focus on line CD.
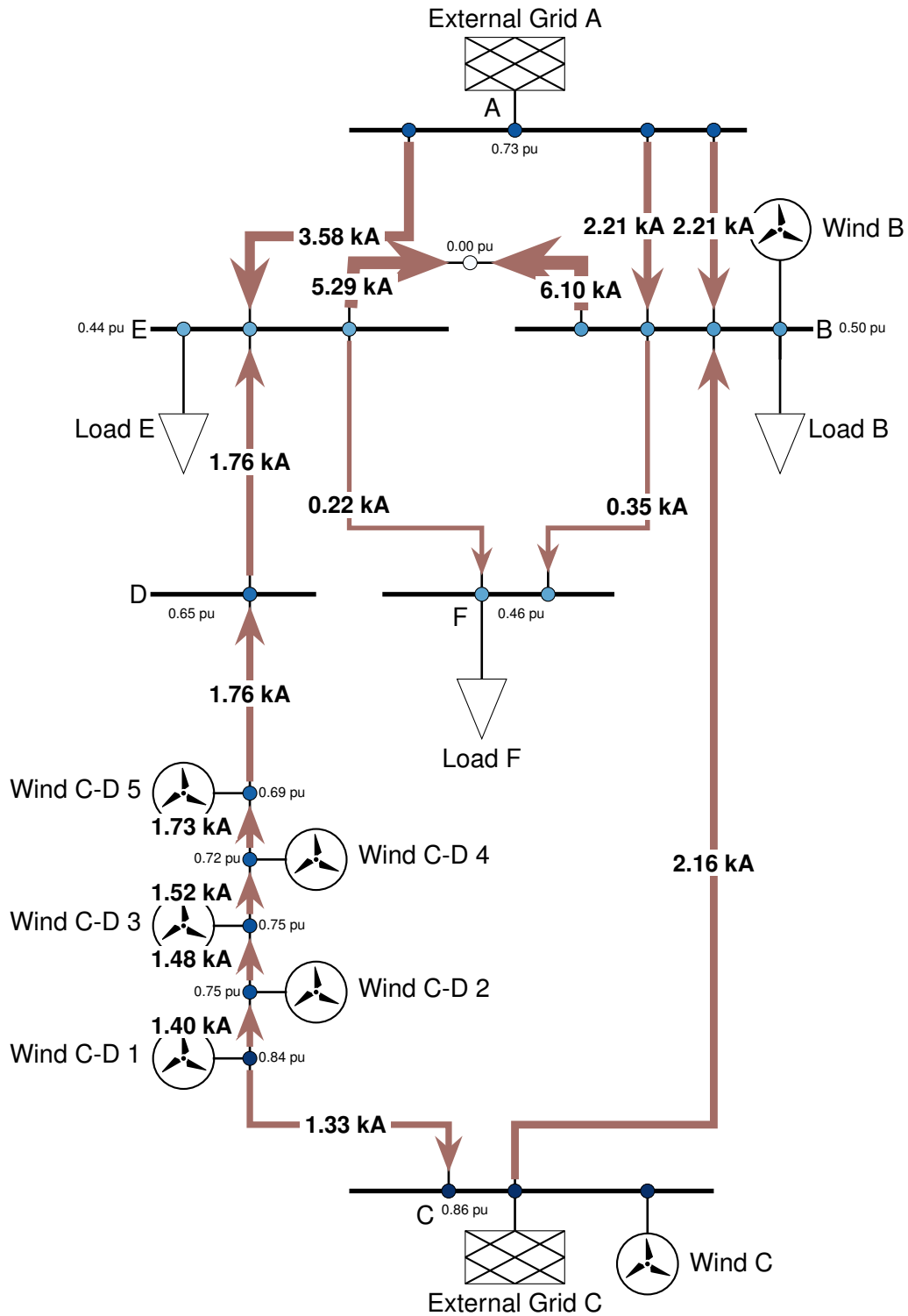
Figure 5.5: Visualization of initial short-circuit current with the fault located at the midpoint of line BE. The bus voltage and current magnitude is marked, with the arrow direction indicating current direction and the arrow thickness indicating the strength of the current.

5.3 Impact of Grid Configuration on Protection Performance

5.3.1 Infeed Effect and Meshed Network Topology

This section supplements the explanation of the infeed impact. To isolate the impact of wind generation, the network under the Case 2 (No wind generators) configuration is simulated. The resulting fault case ratio trend is illustrated in Figure 5.6. The fault case ratio shows an obvious reduction with wind generators removed, which is visualized in the "Difference" curve.

In the "Case 2" curve, where wind farms are absent, the observed variance in the fault case ratio is driven solely by the dynamic behavior of the load profile. The peak-to-peak variability drops by 14% compared with the "Case 1" curve, underscoring the dominant role of load dynamics in shaping fault ratio fluctuations. The comparison also shows that the average fault case ratio drops by 4 %, with the number indicating that wind farm infeed contributes a small amount to the apparent impedance distortion compared to infeed current sourced from external grids.

The "Difference" curve further reveals that wind generation introduces intermittent and less predictable variations in the fault case ratio relative to load variance effects. It indicates the complicated point in protection design in high DG penetration grids.
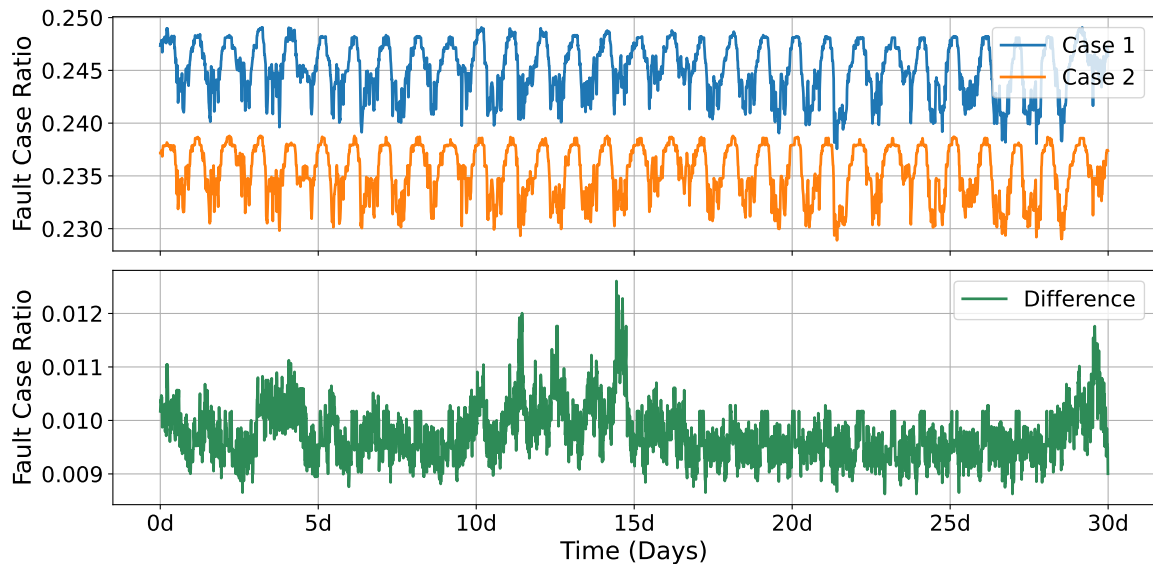
Figure 5.6: Comparison of the fault case ratio between Case 2 (No wind generators) and Case 1 simulation over a month.

The "Difference" curve also shows a strong correlation of the peak and valley values with the wind generation profiles, which is a supplement to the explanation in Section 5.2.1.

5.3.2 Weak vs. Strong External Grids

Analyzing the impact of external grid strength on distance protection is a critical topic for ensuring reliable operation in modern power systems, where networks increasingly interconnect with diverse energy sources, so that weak external grids can happen, especially in remote areas or systems with high renewable penetration. Therefore, a simulation of Case 3 (with weak external grids) is conducted, with the comparison shown in Figure 5.7. The weak external grid configuration leads to an increased average level of the fault case ratio and more pronounced fluctuations compared with the strong one.
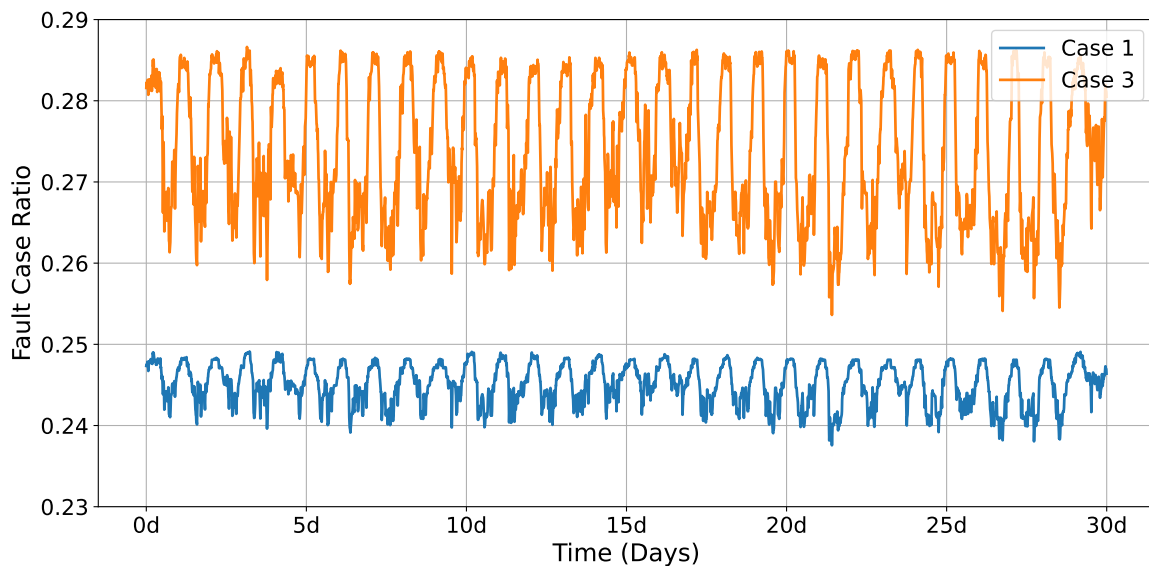
Figure 5.7: Comparison of the fault case ratio between Case 3 (with weak external grids) and Case 1 (with strong external grids) simulation over a month.

The cause of this result is thoroughly analyzed with the help of the fault current illustration in Figure 5.8. Compared with the result under strong external grids in Figure 5.5, the bus voltage and the short-circuit current have a large drop across the network. External grids play a major role in voltage stabilizing, with limited contributions from wind generators. The weaker external grid exhibits a higher internal impedance, reducing its ability to stabilize voltages during faults. On the other hand, the overall fault current magnitude is decreased.

Table 5.3 compares the apparent impedance measurements for device 0 (located at bus A, in the direction of line AE) under both weak and strong external grid conditions, with fault points at varying distances from bus E along line BE.

Table 5.3: The comparison of apparent impedance measurements at different fault distances under weak and strong external grid scenarios (Case 3). Impedance unit: ohm.

Distance (km)	Fault to relay impedance	Strong external grid	Weak external grid
1	0.701+5.461j	0.732+5.630j	0.788+5.681j
20	1.336+10.4010j	2.495+12.733j	4.318+13.928j
39	1.970+15.341j	3.737+15.977j	14.031+16.022j

At a specific fault distance, both configurations show underreach errors, where the measured impedance magnitude under weak external grids is higher and the phase angle shifts further toward the resistive axis.

Figure 5.8 shows that the voltage and the current, which are the two factors affecting the calculation of the apparent impedance, are both dropped. But the ratio, which is the apparent impedance, is increased. Besides the higher internal impedance, weak grids exhibit a higher resistive-to-reactive impedance ratio, shifting the phase angle toward the resistive axis [57]. Moreover, the impedance angle under the weak grid configuration is significantly more sensitive to changes in fault distance. The impedance angle changes from nearly aligned with the line impedance angle to 48° in a small increment of distance. Weak grids amplify angle sensitivity because the internal impedance of the grid combines nonlinearly with the line impedance, causing larger angular deviations for the same distance increment.

The results underscore the critical impact of external grid strength on the distance protection performance and the necessity of a different protection scheme for accurate detections.
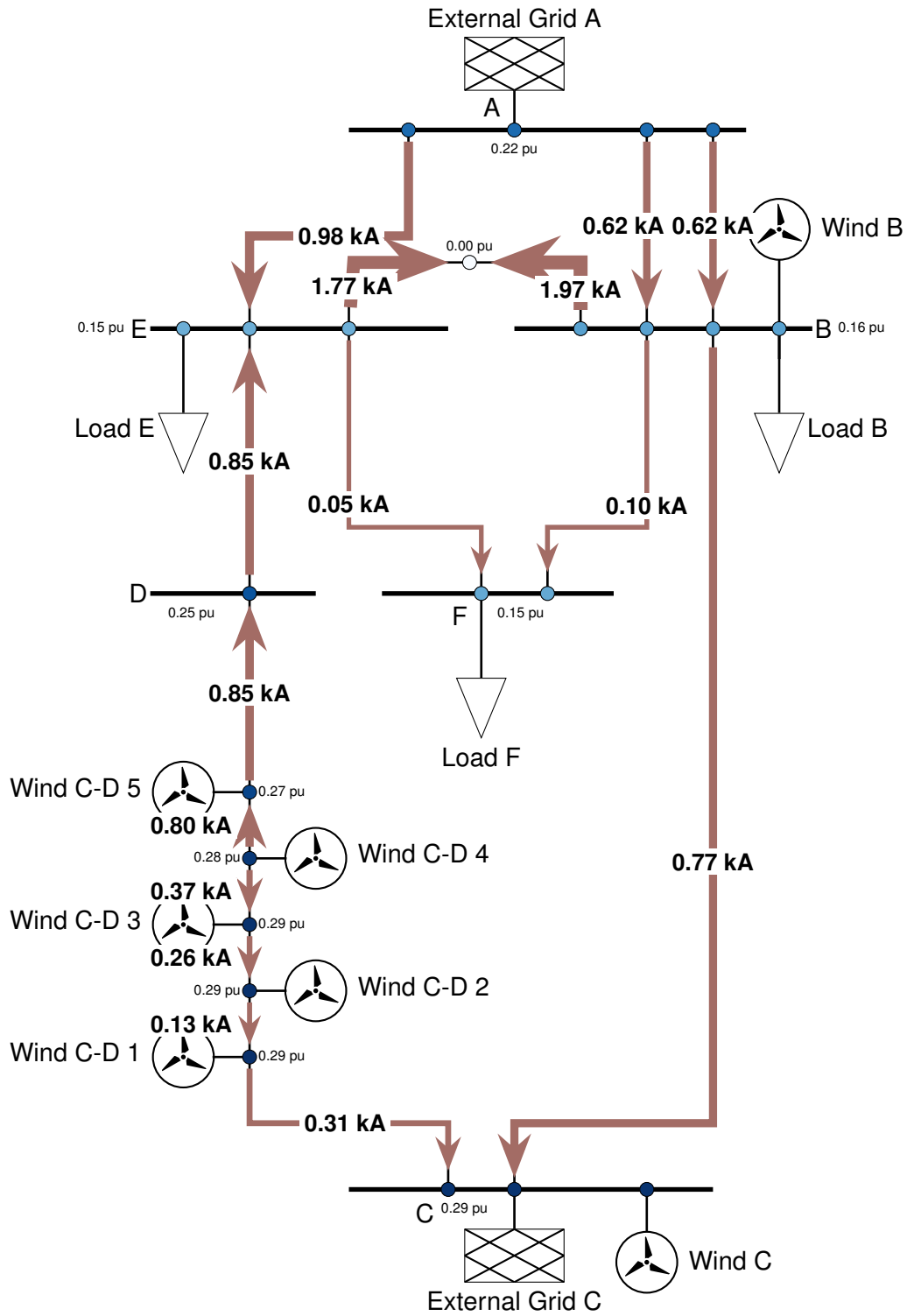
Figure 5.8: Visualization of the initial short-circuit current with the fault located at the mid-point of line BE under weak external grids.

5.4 Distance Protection Performance under Optimized Zones

Zone optimization is a compromise method between adaptive protection and conventional protection, as the zone settings are only once adapted to the measurements for better performance. Figure 5.9 illustrates the comparison of the fault case ratios between Case 1 and Case 4 (optimized zone settings) over a year.

The median fault case ratio is significantly reduced with the new zone settings. In addition to lowering the average ratio, the optimized settings also reduce the fluctuation and outliers within the year, indicating enhanced robustness of the distance protection scheme. This improvement indicates that a well-chosen algorithm may improve the performance at a low cost.
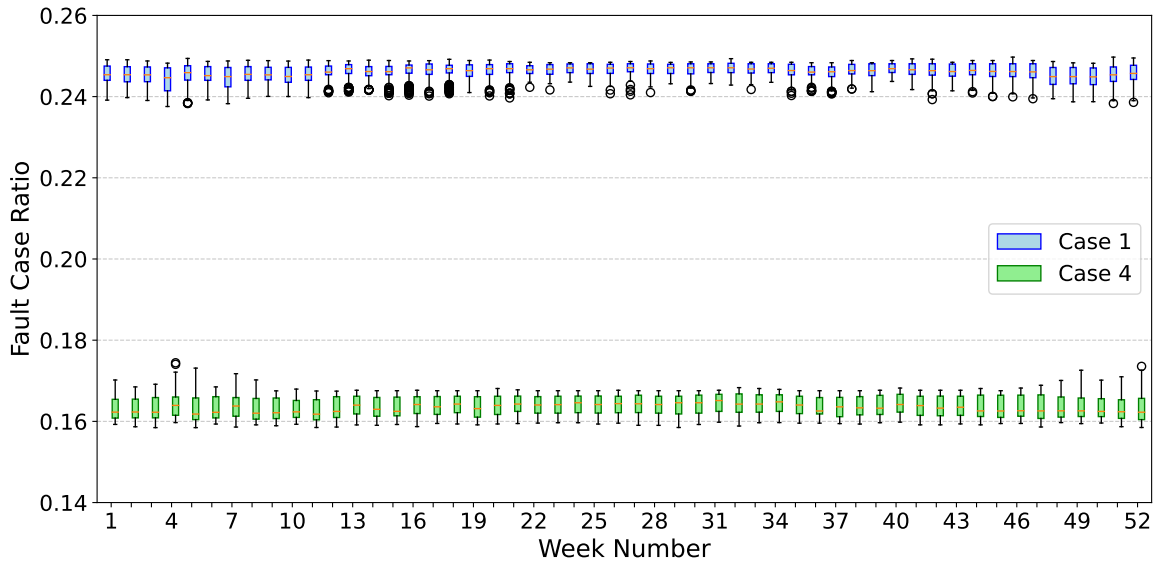
Figure 5.9: Comparison of fault case ratio between Case 4 (optimized zone settings) and Case 1 simulation over a year.

5.5 Evaluation of Underreach and Overreach Fault Cases

After illustrating the results of four cases separately, the underreach and overreach error counts are compared across these cases, as shown in Figure 5.10. Evaluating underreach and overreach errors provides critical insight into the balance between protection selectivity and system security.

Underreach errors, where the relay fails to recognize faults due to an underestimation of the fault proximity, compromise security by leaving faults unresolved, risking equipment damage or cascading failures. Overreach errors lead to premature relay operation, which may trigger unnecessary outages and compromise the overall selectivity by disrupting healthy network sections. Cases 1-3 show a dominant underreach error type, which constitutes over 99 % of total faults, due to the infeed effect. Case 3 (weak external grid) exhibits the highest underreach rate, as reduced fault current contributions and elevated equivalent impedance further distort impedance trajectories. Case 4 (optimized zones) shows that algorithmic optimization reduces underreach errors significantly, improving selectivity by aligning zone boundaries with network-specific infeed problems. However, overreach errors rise as well, introducing security risks.

This trade-off underscores the inherent tension between selectivity and security in static protection schemes.
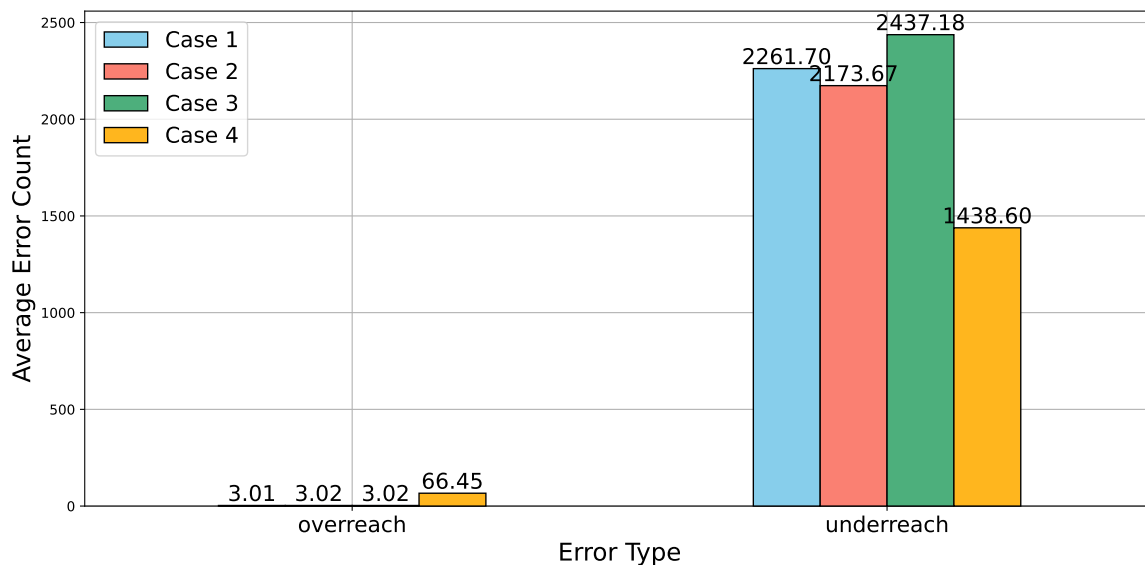
Figure 5.10: Comparison of average underreach and overreach error counts across four cases.

5.6 Discussion of Key Findings

5.6.1 Impact of Dynamic Load and Generation Profiles

When the short-circuit simulation considers the impact of the pre-fault condition, the fault case ratio of the distance protection shows seasonal and daily variations, as shown in Figure 5.1. The curve reveals that error rates tend to be lower and display greater fluctuation during the cold seasons compared with the warm seasons, which is strongly correlated with the dynamic profile patterns. In Section 5.3.1, the impact of faults related to load profiles and generation profiles is separately evaluated. The results indicate that load variations have a more dominant influence on the fault case ratio than wind generation. However, this result is bound to the network topology and network configurations, the relative impact can not be applied generally. Section 5.2.1 evaluates the fault type tendency related to high loading and high generation conditions. Higher loading conditions tend to cause overreach errors, with the apparent impedance magnitude decreased and the angle shifted towards the R axis. The increased wind generation biases the measurements toward underreach conditions, while the increment number of counts is not obviously depicted.

5.6.2 Challenges in Meshed Network Configurations

The analysis shows that meshed network topologies present significant challenges for accurate distance protection. Devices located near junction buses, such as bus B and bus E, encounter complex fault current interactions, as illustrated by the current flow in Figure 5.5. The infeed effect amplifies the impedance between the infeed point and the fault point, which strongly alters the apparent impedance. This effect is more pronounced than the influence of wind generation infeed in this work. Nevertheless, the primary protection is not affected by the meshed topology, which suggests the inadequacy of the backup zone setting of conventional grading methods in such configurations.

5.6.3 Performance of Zones Optimization

The results from the optimization study validate the potential of using static, optimized distance protection parameters to enhance overall system performance, as shown in Figure

5.9. The static optimization result establishes an example for future adaptive schemes, which could dynamically adjust settings in response to real-time grid conditions, further increasing accuracy. However, this improvement introduces a security trade-off: Overreach errors rise significantly from total faults according to Figure 5.10. While conventional grading is more conservative in the infeed compensation, leading to a high ratio of underreach errors, it avoids tripping in healthy network conditions. The result suggests that the zone optimization methods should pay more attention to robust selectivity and adequate security margins rather than accuracy alone.

6 Summary and Outlook

This thesis investigates the accuracy of distance protection in power grids under varying operating conditions, incorporating probabilistic methods to account for uncertainties in load demand, wind generation, and external grid strength. The work aims to address how these factors affect the protection performance, particularly in the example network, where infeed effects present significant challenges.

A 110 kV meshed test network is constructed using the Pandapower toolbox, integrating external grids, loads with real-world load profiles from SimBench, and wind farms, where wind generation data is derived from meteorological observations via the Wetterdienst library (Chapter 4). A custom distance protection class is implemented to evaluate relay decisions with the three-phase short circuit point set at a fixed step in every transmission line. The analysis consists of both dynamic network studies and static network simulation results-based optimization studies (Section 4.1).

The dynamic network assessments are categorized into four simulation cases with a focus on different grid configurations: Baseline operation (Case 1), exclusion of wind generation (Case 2), weak external grid configurations (Case 3), and optimized zone settings (Case 4). Cases 1-3 follow conventional grading settings with the compensation of parallel line cases. Case 4 refines the grading settings with a custom gradient-descent algorithm. The key findings from the simulations are addressed in Section 5.6.

Results highlight that the most significant challenges come from the meshed topologies, with 92% faults concentrated near critical junction buses due to multi-infeed current interactions. Increased loading conditions exacerbate overreach errors due to pre-fault voltage drops, whereas higher wind generation introduces additional infeed currents, resulting in a minor increase in underreach errors (Case 2 vs. Case 1). Results also show that weak external grids exacerbate apparent impedance measurement errors, causing a higher av-

erage fault case ratio and phase angle sensitivity (Case 3 vs. Case 1). The application of the optimization algorithm reduces the overall fault case ratio but introduces a trade-off between sensitivity and security, highlighting the inherent challenges in balancing accurate fault detection with protection reliability (Case 4 vs. Case 1).

The work underscores the limitations of conventional distance protection in grids with high wind generation penetration and complex grid structures. The findings emphasize the need for enhanced protection strategies that consider dynamic grid conditions. Future research could focus on integrating adaptive protection schemes or multiple protection method collaborations to further explore the potential security and selectivity improvements in modern power systems.

Additionally, the simulation framework based on Pandapower developed in this work verifies the feasibility of this tool for time series distance protection system verification and demonstrates its advantages in data visualization. Future work can perform more complex accuracy verification of the short-circuit simulation results generated by Pandapower.

Bibliography

[1] C. Li, Y. Sun, and X. Chen, "Analysis of the blackout in Europe on November 4, 2006," 2007, pp. 939–944.

[2] DNV. (2022) DNV's power failure investigation in the Netherlands reveals special circumstances and provides important learning points.

[3] F. V. Lopes, D. Barros, R. Reis *et al.*, "Methodology for Protection Performance Evaluation on Power Transmission Networks," *IEEE Transactions on Power Delivery*, vol. 33, no. 2, pp. 769–778, Apr. 2018.

[4] M. S. Ballal and A. R. Kulkarni, "Improvements in Existing System Integrity Protection Schemes Under Stressed Conditions by Synchrophasor Technology—Case Studies," *IEEE Access*, vol. 9, pp. 20 788–20 807, 2021.

[5] M. Ghiasi, N. Ghadimi, and E. Ahmadinia, "An Analytical Methodology for Reliability Assessment and Failure Analysis in Distributed Power System," *SN Applied Sciences*, vol. 1, no. 1, p. 44, Nov. 2018.

[6] J. P. Beck, J. Reinhard, K. Kamps *et al.*, "Model Experiments in Operational Energy System Analysis: Power Grid Focused Scenario Comparisons," *Renewable and Sustainable Energy Reviews*, vol. 164, p. 112550, Aug. 2022.

[7] L. Thurner, A. Scheidler, F. Schafer *et al.*, "pandapower - an Open Source Python Tool for Convenient Modeling, Analysis and Optimization of Electric Power Systems," *IEEE Transactions on Power Systems*, 2018. [Online]. Available: https://arxiv.org/abs/1709.06743

[8] N. E. Naily, Saad. M. Saad, Reda. E. Elsayed *et al.*, "Planning & Application of Distance Relays Coordination for IEC Microgrid Considering Intermediate In-Feed Factor," Mar. 2018, pp. 1–6.

[9] D. Oeding and B. R. Oswald, *Elektrische Kraftwerke und Netze*. Berlin, Heidelberg: Springer, 2011.

[10] M. Biller, J. Jaeger, I. Mladenovic *et al.*, "Protection systems in distribution grids with variable short-circuit conditions," 2016, pp. 1–5.

[11] R. Jain, Y. N. Velaga, K. Prabakar *et al.*, "Modern Trends in Power System Protection for Distribution Grid with High DER Penetration," *e-Prime - Advances in Electrical Engineering, Electronics and Energy*, vol. 2, p. 100080, Jan. 2022.

[12] P. LEDU, "PMU Based Real Time Vulnerability Assessment of Zone 3 Distance Relay to Prevent Cascading Outages," 2016.

[13] A. V. Mokeev and S. A. Piskunov, "Improvement of Distance Protection Algorithms Based on Phasor Measurements," *E3S Web of Conferences*, vol. 384, p. 01017, 2023.

[14] F. Hariri and M. Crow, "New Infeed Correction Methods for Distance Protection in Distribution Systems," *Energies*, vol. 14, no. 15, p. 4652, Jan. 2021.

[15] S. Azizi, M. Sanaye-Pasand, and M. Paolone, "A Modified Formula for Distance Relaying of Tapped Transmission Lines With Grounded Neutrals," *IEEE Transactions on Power Delivery*, vol. 34, no. 2, pp. 690–699, Apr. 2019.

[16] P. Lytaev, "Adaptive and Automated Distance Protection in Distribution Grids with High Distributed Generation," 2022. [Online]. Available: https://publica.fraunhofer.de/handle/publica/429349

[17] S. Wang, J. Li, T. Li *et al.*, "An On-line Setting Self-adaptive Distance Protection Scheme for 110kV Transmission Line," Oct. 2020, pp. 2027–2031.

[18] Y. Liang, W. Li, Z. Lu *et al.*, "A New Distance Protection Scheme Based on Improved Virtual Measured Voltage," *IEEE Transactions on Power Delivery*, vol. 35, no. 2, pp. 774–786, Apr. 2020.

[19] O. D. Naidu, N. George, S. Zubic, and M. Krakowski, "Time-Domain-Based Distance Protection for Transmission Networks: Secure and Reliable Solution for Complex Networks," *IEEE Access*, vol. 11, pp. 104 656–104 675, 2023.

[20] A. M. Tsimtsios, G. N. Korres, and V. C. Nikolaidis, "A Pilot-Based Distance Protection Scheme for Meshed Distribution Systems with Distributed Generation," *International Journal of Electrical Power & Energy Systems*, vol. 105, pp. 454–469, Feb. 2019.

[21] S. Paladhi and A. K. Pradhan, "Adaptive Distance Protection for Lines Connecting Converter-Interfaced Renewable Plants," *IEEE Journal of Emerging and Selected Topics in Power Electronics*, vol. 9, no. 6, pp. 7088–7098, Dec. 2021.

[22] V. Terzija and H.-J. Koglin, "On the modeling of long arc in still air and arc resistance calculation," *IEEE Transactions on Power Delivery*, vol. 19, no. 3, pp. 1012–1017, 2004.

[23] A. R. van C. Warrington, "Distance Relays," in *Protective Relays: Their Theory and Practice*. Boston, MA: Springer US, 1968, pp. 191–272.

[24] C. R. Mason, *The Art and Science of Protective Relaying*. New York: John Wiley and Sons, Inc., 1956.

[25] J. L. Blackburn, *Protective Relaying: Principles and Applications*. New York: Marcel Dekker, Inc., 1987.

[26] W. A. Elmore, *Protective Relaying: Theory and Applications*, 2nd ed. Boca Raton: CRC Press, Sep. 2003.

[27] G. Zeigler, *Numerical Distance Protection: Principles and Applications*, 4th ed. Wiley, 2011.

[28] V. D. Andrade and E. Sorrentino, "Typical expected values of the fault resistance in power systems," 2010, pp. 602–609.

[29] J. Ma, X. Yan, B. Fan *et al.*, "A Novel Line Protection Scheme for a Single Phase-to-Ground Fault Based on Voltage Phase Comparison," *IEEE Transactions on Power Delivery*, vol. 31, no. 5, pp. 2018–2027, 2016.

[30] Y. Liang, Z. Lu, W. Li *et al.*, "A Novel Fault Impedance Calculation Method for Distance Protection Against Fault Resistance," *IEEE Transactions on Power Delivery*, vol. 35, no. 1, pp. 396–407, Feb. 2020.

[31] G. M. Gomes Guerreiro, R. Sharma, F. Martin *et al.*, "Concerning Short-Circuit Current Contribution Challenges of Large-Scale Full-Converter Based Wind Power Plants," *IEEE Access*, vol. 11, pp. 64 141–64 159, 2023.

[32] International Electrotechnical Commission (IEC) Std. IEC 60 909-0, 2016.

[33] I. Kasikci, *Definitions: Methods of Calculations*. John Wiley Sons, Ltd, 2018. [Online]. Available: https://onlinelibrary.wiley.com/doi/abs/10.1002/9783527803378.ch1

[34] M. Kolcun, M. Kanálik, D. Medved', and Z. Čonka, "Measuring of Real Value of Short-Circuit Power in Island Operation Condition," May 2015, pp. 418–422.

[35] D. Sweeting, "Applying IEC 60909, Fault Current Calculations," *IEEE Transactions on Industry Applications*, vol. 48, no. 2, pp. 575–580, Mar. 2012.

[36] E. Muljadi and V. Gevorgian, "Short-Circuit Modeling of a Wind Power Plant." San Diego, CA: IEEE, Jul. 2011, pp. 1–9.

[37] A. Heyduk and J. Joostberens, "Comparative Analysis of European and American Standards for Maximum Fault Current Calculations on Medium Voltage Mine Power Networks," *Elektronika ir Elektrotechnika*, vol. 22, no. 2, pp. 13–20, Mar. 2016.

[38] V. C. Nikolaidis, A. M. Tsimtsios, and A. S. Safigianni, "Investigating Particularities of Infeed and Fault Resistance Effect on Distance Relays Protecting Radial Distribution Feeders With DG," *IEEE Access*, vol. 6, pp. 11 301–11 312, 2018.

[39] P. S. Jagtap and M. P. Thakre, "Effect of Infeed Current and Fault Resistance on Distance Protection for Teed-Feed Line," Sep. 2020, pp. 1–6.

[40] Y. Xia, A. David, and K. Li, "High-Resistance Faults on a Multi-Terminal Line: Analysis, Simulated Studies and an Adaptive Distance Relaying Scheme," *IEEE Transactions on Power Delivery*, vol. 9, no. 1, pp. 492–500, Jan. 1994.

[41] M. R. Araújo and C. Pereira, "Influence of Mutual Coupling Modelling on the Effectiveness of a Distance Relaying Algorithm Applicable to Long Parallel Transmission Lines," *The Journal of Engineering*, vol. 2018, no. 15, pp. 1043–1047, 2018.

[42] K. M. Silva, J. S. G. Pena, H. D. M. Braz, and M. Kezunovic, "An Algorithm to Mitigate the Infeed Effect on Overreaching Distance Zones Settings," *IEEE Transactions on Power Delivery*, vol. 37, no. 4, pp. 3345–3356, Aug. 2022.

[43] J. d. J. J. Serna and J. M. López-Lezama, "Calculation of Distance Protection Settings in Mutually Coupled Transmission Lines: A Comparative Analysis," *Energies*, vol. 12, no. 7, 2019.

[44] J. Ma, X. Yan, W. Ma, and L. Sun, "A New Adaptive Distance Protection Scheme for a Transmission Line," *Electric Power Components and Systems*, vol. 44, no. 1, pp. 1–17, Jan. 2016.

[45] J. Ma, X. Xiang, P. Li *et al.*, "Adaptive Distance Protection Scheme with Quadrilateral Characteristic for Extremely High-Voltage/Ultra-High-Voltage Transmission Line," *IET Generation, Transmission & Distribution*, vol. 11, no. 7, pp. 1624–1633, 2017.

[46] U. Uzubi, A. Ekwue, and E. Ejiogu, "An Adaptive Distance Protection Scheme for High Varying Fault Resistances," 2020, pp. 1–5.

[47] R. K. Dubey, S. , Subhransu Ranjan, and B. K. and Panigrahi, "Adaptive Distance Relaying Scheme for Transmission Network Connecting Wind Farms," *Electric Power Components and Systems*, vol. 42, no. 11, pp. 1181–1193, Aug. 2014.

[48] J. Upendar, C. P. Gupta, and G. K. Singh, "Comprehensive Adaptive Distance Relaying Scheme for Parallel Transmission Lines," *IEEE Transactions on Power Delivery*, vol. 26, no. 2, pp. 1039–1052, Apr. 2011.

[49] C. Spalthoff, D. Sarajlic, C. Kittl *et al.*, "SimBench: Open Source Time Series of Power Load, Storage and Generation for the Simulation of Electrical Distribution Grids," May 2019, pp. 1–6.

[50] B. Gutzmann and A. Motl, "wetterdienst," 2023. [Online]. Available: https://github.com/earthobservations/wetterdienst

[51] T. Lorz, J. Jaeger, A. Selimaj *et al.*, "Interconnected Grid Protection Systems - Reference Grid for Testing an Adaptive Protection Scheme," vol. 2023, Jun. 2023, pp. 3286–3290.

[52] V. Project, "VeN2uS: A Research Project on Power Systems." [Online]. Available: https://ven2us.de/

[53] E. W. Dijkstra, "A note on two problems in connexion with graphs," *Numerische Mathematik*, vol. 1, no. 1, pp. 269–271, 1959.

[54] D. W. (DWD), "10-minute station observations of wind for Germany, Version v24.03," 2024. [Online]. Available: https://opendata.dwd.de/climate_environment/CDC/observations_germany/climate/10_minutes/wind/historical/

[55] A. D. Hansen, *Generators and Power Electronics for Wind Turbines*.   John Wiley Sons, Ltd, 2012. [Online]. Available: https://onlinelibrary.wiley.com/doi/abs/10.1002/9781119941842.ch5

[56] S. Ruder, "An overview of gradient descent optimization algorithms," *CoRR*, vol. abs/1609.04747, 2016. [Online]. Available: http://arxiv.org/abs/1609.04747

[57] L. Huang, C. Wu, D. Zhou, and F. Blaabjerg, "Impact of Grid Strength and Impedance Characteristics on the Maximum Power Transfer Capability of Grid-Connected Inverters," *Applied Sciences*, vol. 11, no. 9, p. 4288, Jan. 2021.

List of Figures

# List of Tables

Appendices

A Branched Radial Network Method Explanation

Here is a detailed explanation of the feasibility of setting the downstream distance protection's three zones as the method stated. Figure A.1 illustrates an example consisting of a few protection devices with a hierarchy structure, line a (upstream), line b, c, d (downstream), line e, f, g (another hierarchy downstream). In this net, the transmission lines are assumed to have identical per-unit impedance parameters and follow the relation:

$$Z_b < Z_c < Z_d \qquad\qquad\qquad Z_f < Z_e < Z_g, \tag{A.1}$$

where Z_e, Z_f, and Z_g represent the shortest line segment in their respective hierarchical branches. The assumption is made for calculation simplicity. Following the grading principle, zone 1 of the protection device at the line b, c, d is set to cover 90% of their local lines:

$$dp_{b\_zone1} = 0.9Z_b, \qquad dp_{c\_zone1} = 0.9Z_c, \qquad dp_{d\_zone1} = 0.9Z_d. \tag{A.2}$$
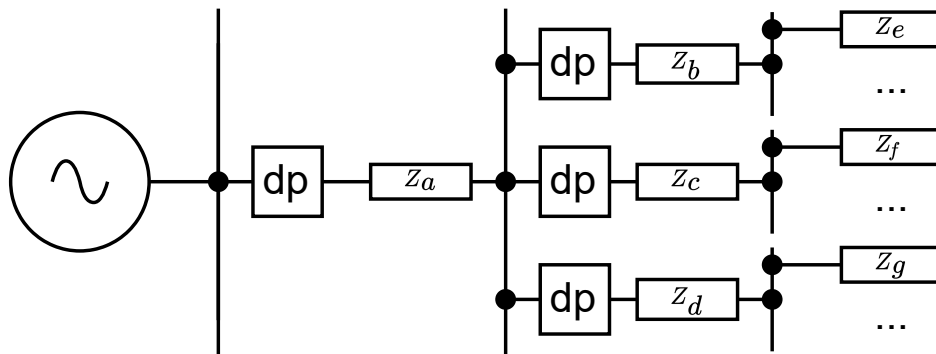
Figure A.1: Distance protection class key architecture.

Zone 2 of them, incorporated with the shortest adjacent line, is set to:

$$dp_{b\_zone2} = 0.9Z_b + 0.81Z_e \tag{A.3}$$

$$dp_{c\_zone2} = 0.9Z_c + 0.81Z_f \tag{A.4}$$

$$dp_{d\_zone2} = 0.9Z_d + 0.81Z_g \tag{A.5}$$

The method describes that the distance protection device chooses the shortest line in the depth 2 search and depth 3 search for zone grading. Therefore, the protection device at line a sets the three zones with:

$$dp_{a\_zone1} = 0.9Z_a \tag{A.6}$$

$$dp_{a\_zone2} = 0.9Z_a + 0.81Z_b \tag{A.7}$$

$$dp_{a\_zone3} = 0.9Z_a + 0.81Z_b + 0.72Z_f \tag{A.8}$$

with the shortest reach principle.

To ensure compliance with the Ziegler grading principles [27], the following inequalities must hold:

1. Zone 2 Selectivity: The upstream relay's Zone 2 must not overreach the downstream relay's Zone 1:

$$dp_{a\_zone2} - Z_a < min(dp_{b\_zone1}, dp_{c\_zone1}, dp_{d\_zone1}) \Rightarrow 0.9Z_a + 0.81Z_b - Z_a < 0.9Z_b \tag{A.9}$$

Simplifying confirms $0.81Z_b < 0.9Z_b$, which holds true for all positive Z_b.

2. Zone 3 Selectivity: The upstream relay's Zone 3 must not overreach the downstream relay's Zone 2:

$$dp_{a\_zone3} - Z_a < min(dp_{b\_zone2}, dp_{c\_zone2}, dp_{d\_zone2}) \tag{A.10}$$

Substituting values:

$$0.9Z_a + 0.81Z_b + 0.72Z_f - Z_a < min(0.9Z_b + 0.81Z_e, 0.9Z_c + 0.81Z_f) \quad \text{(A.11)}$$

Given Equation A.1, it can be obtained:

$$min(0.9Z_b + 0.81Z_e, 0.9Z_c + 0.81Z_f) > 0.9Z_b + 0.81Z_f > 0.81Z_b + 0.72Z_f - 0.1Z_a \quad \text{(A.12)}$$

Feasibility is validated.

B Wind Turbine Power Coefficient

The specification is from WWD-1 wind turbines manufactured by the company WinWinD.

Table B.1: Cp value for different wind speed

Wind Speed	Power coefficient
1	0
2	0
3	0.228
4	0.322
5	0.380
6	0.408
7	0.413
8	0.418
9	0.419
10	0.419
11	0.401
12	0.378
13	0.305
14	0.244
15	0.199
16	0.164
17	0.136
18	0.115
19	0.098
20	0.084
21	0.072
22	0.063
23	0.055
24	0.048
25	0.042
26	0

Using this coefficient, the power curve for the turbine across different wind speeds is constructed, illustrated in Figure B.1. The power output curve starts at the cut-in speed of 3 m/s and gradually increases with wind speed. It reaches its maximum at the rated speed of 13.5 m/s, which represents the highest power output of the turbine. Beyond this point, the

curve remains relatively constant until the cut-out speed of 25 m/s, at which point the turbine stops generating power to prevent damage.
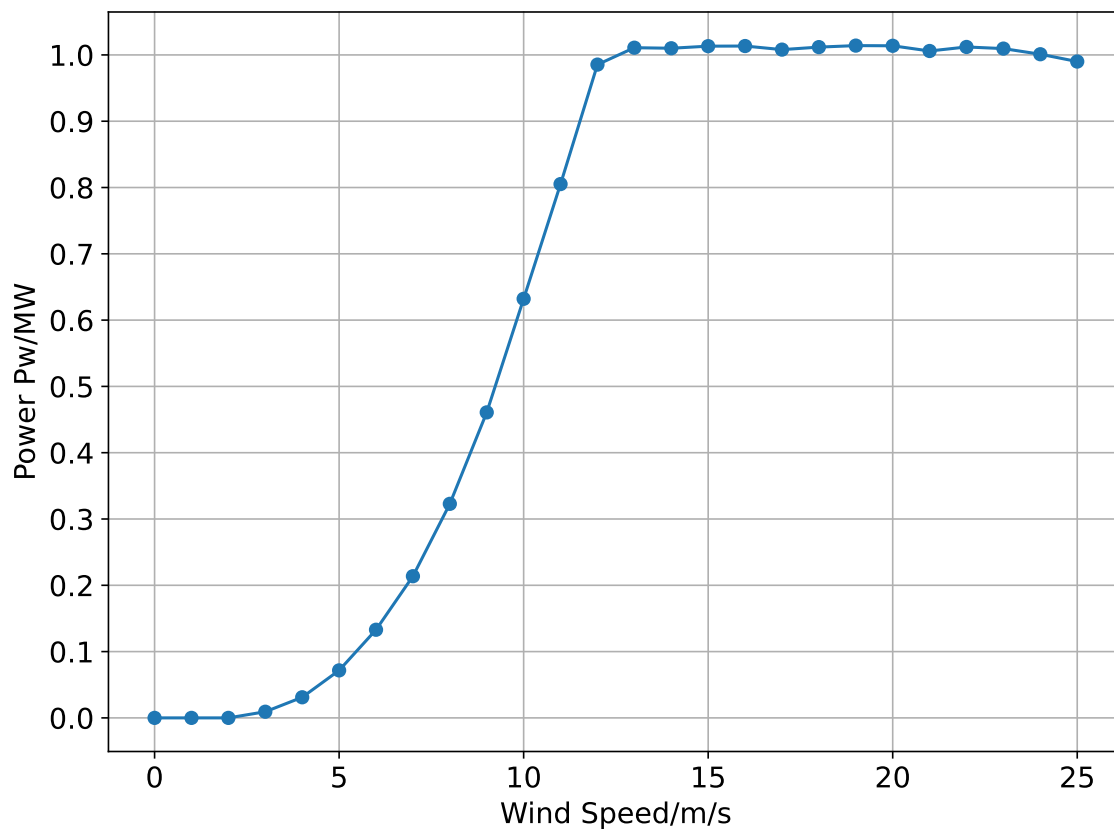
Figure B.1: Power Output vs. Wind Speed.

C Distance Protection Zone Grading Reference Values

The distance protection device zone grading follows the zone grading method described in Section 3.2. Table C.1 gives the reference values for the devices.

Table C.1: Impedance values for each device and zone.

| Device ID	Zone 1 Impedance	Zone 2 Impedance	Zone 3 Impedance
0	$0.601 + 4.680j$	$1.413 + 10.999j$	$1.717 + 13.369j$
1	$0.601 + 4.680j$	$0.977 + 7.606j$	$1.653 + 12.871j$
2	$0.751 + 5.851j$	$1.563 + 12.169j$	$2.050 + 15.960j$
3	$0.751 + 5.851j$	$1.292 + 10.063j$	$2.023 + 15.750j$
4	$0.751 + 5.851j$	$1.563 + 12.169j$	$2.050 + 15.960j$
5	$0.751 + 5.851j$	$1.292 + 10.063j$	$2.023 + 15.750j$
6	$1.202 + 9.361j$	$1.578 + 12.286j$	$2.388 + 18.592j$
7	$1.202 + 9.361j$	$1.743 + 13.573j$	$2.047 + 15.943j$
8	$1.052 + 8.191j$	$1.863 + 14.509j$	$2.168 + 16.879j$
9	$1.052 + 8.191j$	$1.593 + 12.403j$	$1.897 + 14.773j$
10	$0.902 + 7.021j$	$1.277 + 9.946j$	$2.020 + 15.731j$
11	$0.902 + 7.021j$	$1.848 + 14.392j$	$2.335 + 18.184j$
12	$0.902 + 7.021j$	$1.808 + 14.076j$	$2.781 + 21.659j$
13	$0.902 + 7.021j$	$1.443 + 11.233j$	$1.747 + 13.603j$
14	$1.007 + 7.840j$	$2.089 + 16.265j$	$2.393 + 18.634j$
15	$1.007 + 7.840j$	$1.818 + 14.158j$	$2.305 + 17.949j$
16	$1.202 + 9.361j$	$1.578 + 12.286j$	$2.388 + 18.592j$
17	$1.202 + 9.361j$	$2.108 + 16.417j$	$2.839 + 22.103j$

D Wind and Load Profiles Over One Year

The wind power profiles are derived from wind speed estimations at network nodes within the geographic region depicted in Figure 4.2. Given the limited spatial extent of the network (horizontal and vertical distances do not exceed 100 km), wind speed variations across the region are considerably low. The active power generation profiles for all wind farms over a year are illustrated in Figure D.1. The reactive power output is maintained at a constant power factor and is therefore not shown. The temporal trends across wind farms are broadly similar, with noticeable differences in installed capacities.

To resolve finer temporal dynamics, Figure D.2 presents a 10-day subset of the data, smoothed using a Savitzky-Golay filter (3rd-order polynomial, 51-hour window). Data shows small shifts in the peak and valley values.

Load profiles are derived from the SimBench dataset, with scaling factors applied to match the power level. The annual active and reactive power consumption for the load B, as the representative, are illustrated in Figure D.3. The original data fluctuates significantly, so a smoothing filter Locally Weighted Scatterplot Smoothing (Lowess) is applied to highlight trends. The load is higher and more variable during winter months compared to summer.
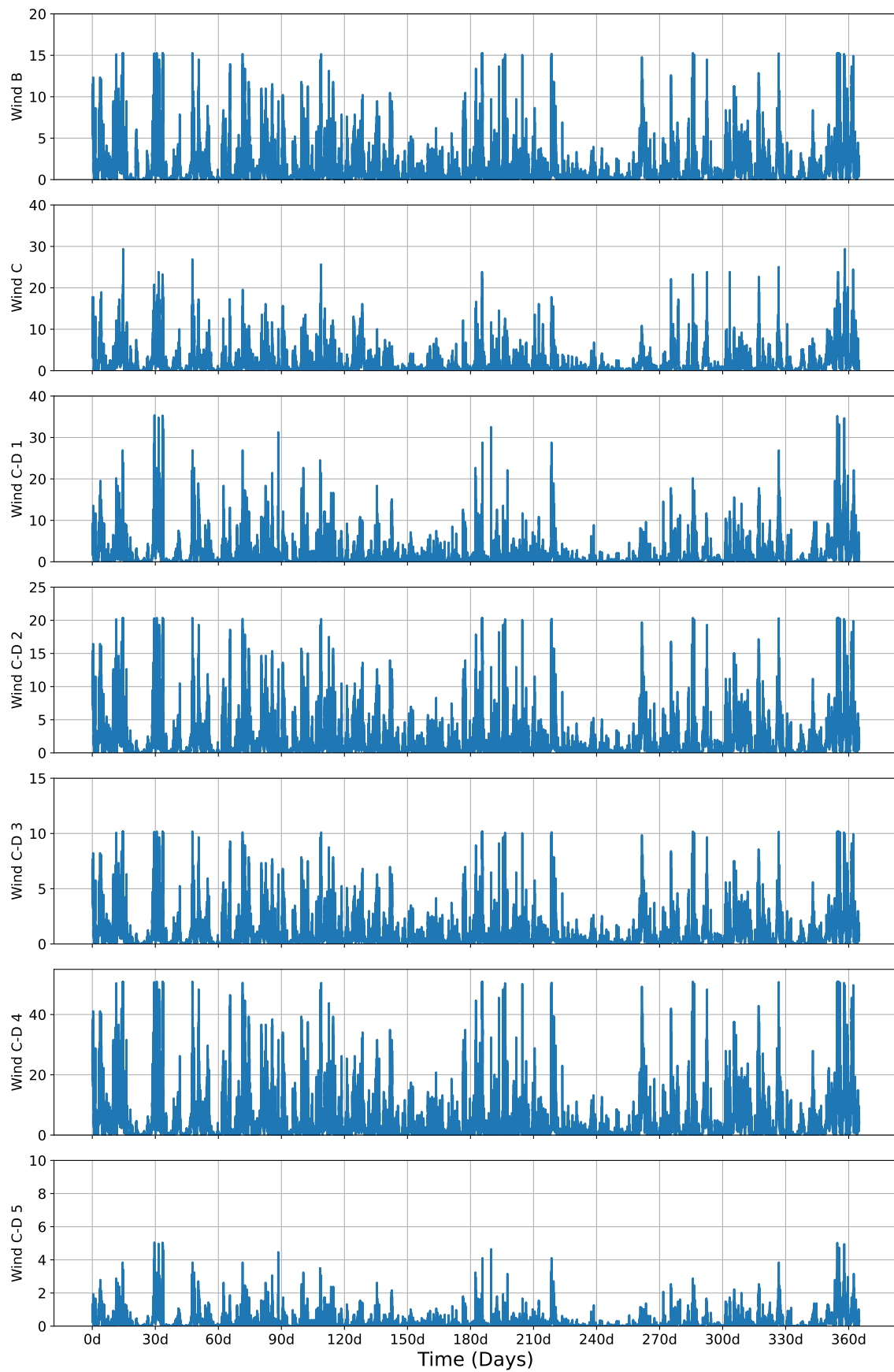
Figure D.1: Active power output (MW) of the wind farms over a year.
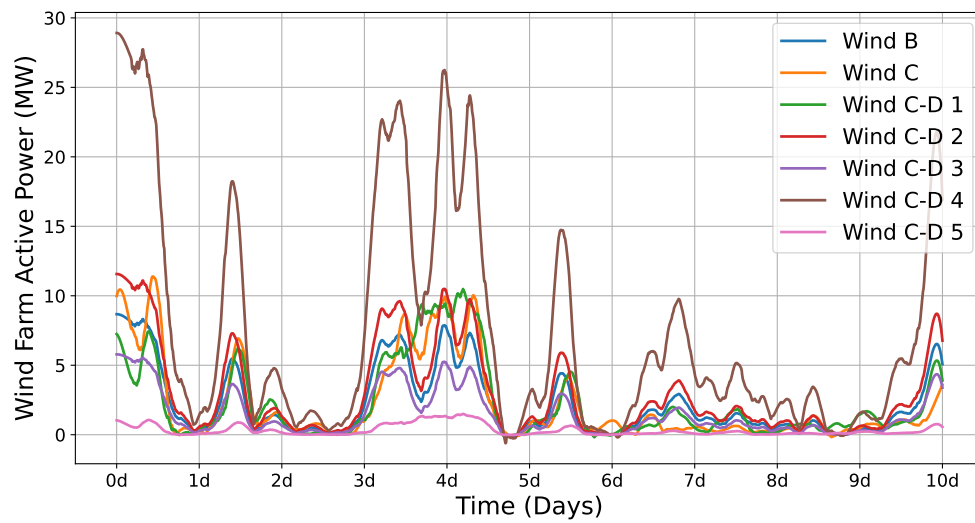
Figure D.2: Short-term wind active power output comparison, smoothed via Savitzky-Golay filter.
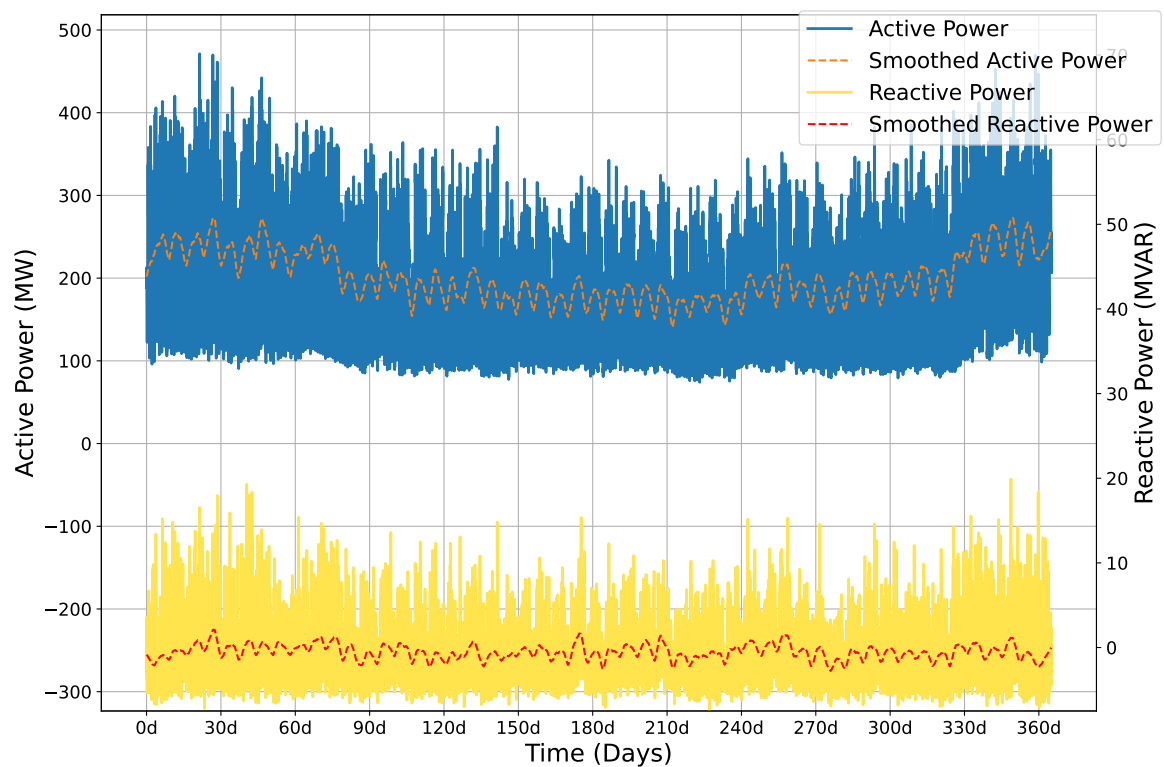
Figure D.3: Active power and reactive power consumption of representative load B over one year.

Eidesstattliche Erklärung

Hiermit erkläre ich, Zhao Ming, dass ich die vorliegende Masterarbeit selbstständig und nur unter Verwendung der angegebenen Literatur und Hilfsmittel angefertigt habe. Die aus fremden Quellen direkt oder indirekt übernommenen Stellen sind als solche kenntlich gemacht. Die Arbeit wurde bisher in gleicher oder ähnlicher Form keiner anderen Prüfungs- behörde vorgelegt und auch nicht veröffentlicht.

Hamburg, 22nd April 2025

_____

Zhao Ming